Asteroseismology of 16 Cyg A and B

João Pedro de Sousa Faria
Mestrado em Astronomia
Departamento de Física e Astronomia
2013

Orientador
Mário João Pires Fernandes Garcia Monteiro,
Professor Associado, Faculdade de Ciências da Universidade do Porto

Coorientador
Margarida Maria Salvador Cunha,
Investigadora Principal, Centro de Astrofísica da Universidade do Porto

Centro de Astrofísica
da Universidade do Porto

U.PORTO

FC FACULDADE DE CIÊNCIAS
UNIVERSIDADE DO PORTO

Todas as correções determinadas pelo júri, e só essas, foram efetuadas.

O Presidente do Júri,

Porto, 11 / 11 /2013

Acknowledgments

This work would not have been possible without the help and guidance of my supervisors, Dr. Mário João Monteiro and Dr. Margarida Cunha. I would like to express my sincere gratitude to both. Besides being outstanding researchers, they have proven to be remarkable teachers and their expertise, insight, and patience added considerably to my experience. I was lucky to learn how to do science from two of the best scientists I know.

The following, more personal, acknowledgments have no need to be in English.

Sem a ajuda generosa e altruísta da minha amiga Brígida, a aventura que foram estes dois anos numa cidade nova, com pessoas novas, com experiências novas, não teria sido sequer imaginável. Um sincero obrigado, pelo apoio e pela amizade.

Por último, gostaria de agradecer à minha mãe, por tudo, desde o primeiro dia (na verdade, desde o primeiro dia menos nove meses). Fizeste tudo bem, à primeira tentativa.

Abstract

The *Kepler* space telescope has produced very precise long-term photometric time series data for thousands of stars in its quest to find planets similar to Earth. The data allowed the detection of solar-like oscillations in a wide range of stellar types, from giants to subdwarfs. Stellar oscillations allow us to improve structure and evolution models because they are the only observables probing the internal properties of stars.

The correct use of all the information contained in the oscillation frequencies can provide very precise estimates of the masses, radii, ages and chemical abundances of stars. The study of the available diagnostics tools that use only data that can be observed in stars other than the Sun is thus valuable in order to explore the full potential of current and future observations.

In this work, I focus on two particular sources, the components of the 16 Cyg binary, and use asteroseismic tools to extract information about their interior regions. I perform model fitting of the observed frequencies and investigate the so called acoustic glitches – regions with an abrupt change in the stratification of the star – and their effect on the observed oscillation frequencies.

Keywords. asteroseismology – stars: solar-type – stars: evolution – stars: interiors – stars: oscillations – methods: data analysis

Resumo

O telescópio espacial *Kepler*, na sua demanda por planetas similares à Terra, obteve séries temporais de fotometria para milhares de estrelas, com uma precisão e duração inéditas. Estes dados permitiram a deteção de oscilações do tipo solar em estrelas com uma vasta gama de tipos espectrais. O estudo destas oscilações, que são os únicos observáveis que transportam informação detalhada sobre o interior das estrelas, permite melhorar os modelos de estrutura e evolução estelar.

A correcta utilização de toda a informação contida nas frequências de oscilação pode levar a determinações bastante precisas da massa, raio, idade e abundâncias químicas das estrelas. O estudo das ferramentas de diagnóstico dos interiores estelares que precisam apenas do mesmo tipo de dados que são observáveis noutras estrelas é, então, uma mais valia na exploração de todo o potencial das observações presentes e futuras.

Neste trabalho, focado nos componentes do binário 16 Cyg em particular, estudo algumas aplicações dos dados de asterosismologia para extrair informação sobre as regiões interiores destas estrelas. Modelos de evolução estelar são ajustados às frequências observadas e os chamados *acoustic glitches* – regiões onde a estratificação da estrela muda bruscamente – bem como as formas de os detectar são também estudados.

Palavras-chave. asterosismologia – estrelas: tipo solar – estrelas: evolução – estrelas: interiores – estrelas: oscilações – métodos: análise de dados

Contents

List of Figures

In all figures where it applies and is not stated otherwise, we use the following symbol and color convention:

$\ell = 0$ points represented by red stars

$\ell = 1$ points represented by green circles

$\ell = 2$ points represented by blue diamonds

$\ell = 3$ points represented by magenta squares.

List of Tables

Listings

The MESA inlist files and open-source versions of both detection methods are available online at https://www.astro.up.pt/~jfaria/msc-thesis.

1

Introduction

It is becoming standard practice to cite Eddington in general introductions related to asteroseismology. A standard from which I will not deviate:

> *Ordinary stars must be viewed respectfully like objects in glass cases in museums; our fingers are itching to pinch them and test their resilience. Pulsating stars are like those fascinating models in the Science Museum provided with a button which can be pressed to set the machinery in motion. To be able to see the machinery of a star throbbing with activity is most instructive for the development of our knowledge.*
>
> – A.S. Eddington, Stars and Atoms, Oxford University Press, 1927

Asteroseismology is the science that studies the internal structure of pulsating stars by interpreting their frequency spectra. The size, temperature and brightness of these stars vary periodically by a very small but measurable amount (a fraction of a degree in temperature and a few parts per million in brightness, for a star like the Sun). These variations will also cause radial velocity and line profile changes. Therefore, pulsating stars can be studied photometrically and spectroscopically, with time series measurements. By performing a frequency analysis of the time series it is possible to identify oscillation patterns, often with a large number of dominant frequencies (see Figure 1.1).

Different frequencies correspond to different oscillation modes that provide information about the interior regions of the star because they are the surface manifestations of sound waves trapped inside the star.

In a manner that is very similar to how a seismologist uses earthquakes to probe the interior of the Earth, an asteroseismologist probes the interior of stars by studying their natural oscillation modes.

One difference to geoseismology is that the surfaces of stars other than the Sun are not resolved by current observations, which means that inference about the stellar interiors needs to rely on oscillation modes that do not cancel out when disk-integrated measurements are made. The modes of spherically symmetric stars are characterized by eigenfunctions that are proportional to the spherical harmonics $Y_{\ell m}$ with the quantum numbers obeying $\ell = 0, 1, 2, \dots; m = 0, \pm 1, \dots, \pm \ell$. The angular degree ℓ corresponds

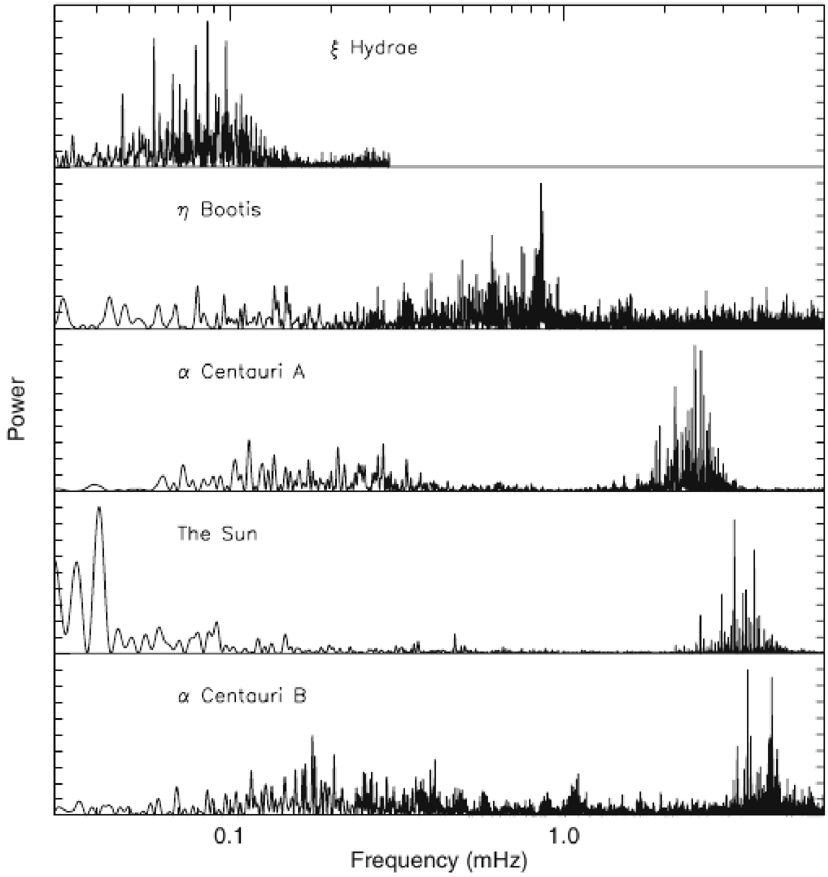

Fig. 1.1 - Power spectra of solar-like oscillations for representative stars. The plots are organized in the order of decreasing mean density from bottom to top, and shown on the same frequency scale. From Cunha et al. [2007, and references therein]

to the number of surface nodes of the oscillation. Only modes with small angular degrees ($\ell \leq 3$) can currently be detected in stars other than the Sun.

The Sun is the best known of all the stars and, as a consequence, is used as a reference in many astronomical works. Results from solar astrophysics and in particular the seimic study of the Sun, Helioseismology, already provide a clear understanding of what happens inside the Sun, [Gough and Toomre, 1991, Christensen-Dalsgaard, 2002] but the theory of stellar structure and evolution has to rely on more than just one observational point. This is why it is important to study other stars, in different evolutionary stages, with different masses, chemical compositions, etc.

A natural follow up from solar studies are solar-type stars, i. e., stars that share some characteristics with the Sun. Apart from the intrinsic interest in studying the fate and past of stars with one solar mass, it is also easier to extrapolate some physical concepts, which many times depend on poorly constrained parameters, to stars in which we expect the same physical processes to take place with similar relative importance.

The precise data available from space missions like *Kepler*[†] [Gilliland et al., 2010] has made possible asteroseimic investigations that cover a broad range of stellar properties and evolutionary stages. In particular, the clear detection of dozens of oscillation frequencies on distant solar-like stars [e. g. Chaplin et al., 2011] has provided a means to study their interiors, which seemed inaccessible before. However, it has also exposed some issues with current state of the art stellar models.

The modelling of the near-surface regions of a solar-like star is still deficient as it ignores dynamical effects of convection. Also, frequency calculations are almost always carried out in the adiabatic approximation, even though the oscillations are definitely not in this regime in the superficial layers [e. g. Houdek, 2010]. These and other uncertainties in stellar modelling mean that the naive comparison between observed values of frequencies and those computed from models will not be an optimal procedure, despite its simplicity. This is because it is affected by a global average of all the uncertainties, even if some are not pertinent to a particular calibration.

There are three different ways to circumvent these difficulties: *a)* apply a correction to the model frequencies that can eliminate the systematic differences to the observations [Kjeldsen et al., 2008] and carry on with the search for the best fitting model parameters; *b)* Consider combinations of frequencies constructed in such a way that they will be insensitive to certain aspects of the stellar modeling, and compare those with observed values calculated in the same manner; *c)* rely on properties of the frequencies (or of the frequency combinations) that depend only on a very specific region of the star, for which an example may be the oscillatory signals produced in the frequencies by regions of rapid variation of the stellar structure, the so called acoustic glitches [Gough, 1990].

In this work I study the last two options and use them to extract detailed information about the interiors of two particular stars, the components of the binary system 16 Cygni. Binaries are important science cases because one can usually decrease the degrees of freedom of the problem, assuming identical initial chemical compositions and ages for both stars of the system. Being very bright targets, the quantity and quality of available data for the two stars are also exquisite.

Several frequency combinations, that extend beyond the more common large and small separations will be discussed and used to improve the forward modelling approach. They are applied to the 16 Cygni data and an inference is made on the best model parameters for each star, building on results of previous works [Metcalfe et al., 2012]. The best models are expected to reproduce well the interior regions of the stars.

[†] There has been no space telescope completely dedicated to asteroseismology, though the French-led CoRoT mission stated it as one of its core objectives [e. g. Baglin et al., 2007]. *Kepler* was launched in 2009, and although originally designed to search for earth-like planets, it has been very effective in performing asteroseismic measurements, providing extremely precise and long time series photometry for hundreds of stars.

To obtain the stellar models I will be using a fairly recent stellar evolution code, MESA (Modules for Experiments in Stellar Astrophysics, [Paxton et al., 2011, 2013]). The code is completely open-source and has already built a community of users, which provides a fair amount of technical support and encourages sharing and reproducibility of results. Despite being open-source MESA is not, by all means, simple. It is a fully modular code that uses comprehensive and up-to-date microphysics and solves the structure and evolution equations with modern techniques, targeted at modern computers. MESA STAR is the name of the stellar evolution code itself that makes use of all the physics and mathematics modules to build and evolve stellar models. For the calculation of oscillation frequencies for the models, MESA has been integrated with ADIPLS, the Aarhus adiabatic oscillation package [Christensen-Dalsgaard, 2008].

A second part of this work is focused on the oscillatory signals present in the oscillation frequencies that are caused by the rapid structural variations at the base of the convection zone and at the Helium second ionization region (from now on, *BCZ* and *HeIIZ*, respectively). By detecting and characterizing these signals one can expect to constrain not only the position of the corresponding regions inside the star but also other stellar parameters related to the physical cause of the signals, such as the surface Helium abundance. For the Sun, this has been extensively studied before [Monteiro and Thompson, 2005, and references therein] and for other stars the best methods are still being developed [Mazumdar et al., 2012]

The end goals of this thesis are the construction of models that reproduce the observed characteristics of the two stars, the detailed description of the acoustic glitches and their effect on the oscillation frequencies, as well as the description of the methods used to detect them and how they can be used to calibrate the surface Helium abundance of 16 Cyg A & B. The dissertation is organized as follows: in the following chapter (Chapter 2) the theoretical basis of asteroseismology of solar-type stars is briefly reviewed and the frequency combinations that can be used as diagnostics of the stellar interiors are presented and justified. Chapter 3 introduces acoustic glitches, the reasons for the presence of an oscillatory signal in the frequencies and the methods used to detect this signal. Our own implementations and improvements to these methods are described in detail and validated using solar data. In Chapter 4 the main focus is drawn to 16 Cyg A & B, the available *Kepler* data is listed together with the results obtained for the modelling and the acoustic glitch characterization. Preliminary results on an attempt to calibrate the Helium surface abundance are presented next and in Chapter 5, I discuss the main results and draw some final conclusions.

2

Stellar Oscillations and Diagnostic Tools

From a theoretical perspective, we start by understanding where the diagnostic potential of stellar oscillations comes from. With only a few assumptions about the equilibrium background state of the star, which is perturbed to obtain a basic description of the oscillations, we can already grasp some of the dependence of the oscillation frequencies on the stellar interior. This theoretical description will allow for an interpretation of the observed frequencies.

In this chapter a brief introduction to the theory of stellar oscillations is presented, together with some results from the asymptotic theory. The expressions for different frequency combinations are also shown and will serve as diagnostic tools to probe specific regions of the stellar interior.

2.1 Basic Oscillation Equations

The adiabatic oscillations of a spherically symmetric star are described by the standard equations of fluid mechanics

$$\begin{aligned} \rho\frac{d\mathbf{u}}{dt} + \nabla P + \rho\nabla\Phi &= 0 \qquad &&\text{(equation of motion)} \\ \frac{d\rho}{dt} + \rho\nabla\cdot\mathbf{u} &= 0 &&\text{(mass conservation)} \\ \frac{1}{p}\frac{dP}{dt} - \frac{\Gamma_1}{\rho}\frac{d\rho}{dt} &= 0 &&\text{(adiabatic condition)} \\ \nabla^2\Phi &= 4\pi G\rho &&\text{(Poisson's equation)} \end{aligned} \tag{2.1}$$

where $\mathbf{u}$, P, ρ, Φ, Γ_1 are the velocity, pressure, density, gravitational potential and first adiabatic exponent, respectively. The derivative following the motion of the gas, $d/dt = \partial/\partial t + \mathbf{u}\cdot\nabla$, is the Lagrangian (or material) time derivative. This *Lagrangian* form of the equations is often used since it simplifies some of the equations. The adiabatic condition results from the energy equation when we consider that no heat is exchanged during the oscillations.

If there are no velocities and the system is static, so that $\mathbf{u} = 0$ and all time derivatives can be neglected, we say the system is in equilibrium and equations (2.1) reduce to the equations of the hydrostatic structure of a spherical star

$$\frac{dp_0}{dr} = -g\rho_0, \qquad g = \frac{d\Phi_0}{dr} = \frac{GM_r}{r^2}, \qquad \frac{dM_r}{dr} = 4\pi G\rho_0 r^2$$

with M_r the mass inside a sphere with radius r and G the gravitational constant. Here, we use the subscript 0 (zero) to refer to the equilibrium structure.

Considering small amplitude perturbations around the equilibrium state we write

$$\mathbf{u} = \frac{d(\delta\mathbf{r})}{dt}, \qquad p = p_0 + p', \qquad \rho = \rho_0 + \rho', \qquad \Phi = \Phi_0 + \Phi'$$

where quantities with a superscript are small, time dependent, Eulerian perturbations. Note that the perturbations are not necessarily spherically symmetric. We seek solutions for the perturbations with time dependence given by $e^{i\omega t}$, with a frequency ω. Given the assumption that the equilibrium state is spherically symmetric, the dependence of the perturbations on the angular variables (θ, ϕ) can be separated from that on the radial variable r by means of spherical harmonics $Y_{\ell m}$. Here, ℓ and m are integers such that $\ell \geq 0$ and $|m| \leq \ell$. We then write the perturbations as

$$\begin{aligned} \delta\mathbf{r} &= \left(\xi(r), \zeta(r)\frac{\partial}{\partial\theta}, \zeta(r)\frac{\partial}{\sin\theta\partial\phi}\right) Y_{\ell m} e^{i\omega t} \\ p' &= \tilde{p}(r) Y_{\ell m} e^{i\omega t} \\ \Phi' &= \tilde{\Phi}(r) Y_{\ell m} e^{i\omega t} \end{aligned} \tag{2.2}$$

allowing us to write the equations of small amplitude adiabatic oscillations

$$\begin{aligned} \frac{d\xi}{dr} + \left(\frac{2}{r} - \frac{g}{c^2}\right)\xi + \left(1 - \frac{S_l^2}{w^2}\right)\frac{p'}{\rho c^2} - \frac{\ell(\ell+1)}{w^2 r^2}\Phi' &= 0 \\ \frac{dp'}{dr} + \frac{g}{c^2}p' + \left(N^2 - w^2\right)\rho\xi + \rho\frac{d\Phi'}{dr} &= 0 \\ \frac{d^2\Phi'}{dr^2} + \frac{2}{r}\frac{d\Phi'}{dr} - \frac{\ell(\ell+1)}{r^2}\Phi' - 4\pi G\rho\left(\frac{p'}{\rho c^2} + \frac{N^2}{g}\xi\right) &= 0 \end{aligned} \tag{2.3}$$

In Eqs. (2.3), we introduced the adiabatic sound speed c given by

$$c^2 = \Gamma_1 \frac{p}{\rho}$$

and two characteristic frequencies: the Lamb (or acoustic) frequency S_ℓ

$$S_\ell^2 = \frac{\ell(\ell+1)c^2}{r^2}$$

and the Brunt-Väisälä (or buoyancy) frequency N

$$N^2 = -\frac{g^2}{c^2}\left(1 - \Gamma_1 \frac{d\log\rho}{d\log p}\right)$$

Note that all the terms in Eqs. (2.3) are independent of m as a consequence of the spherical symmetry of the equilibrium state. This degeneracy is lifted by rotation.

This system of homogeneous equations is of fourth order and must satisfy four boundary conditions at the center ($r = 0$) and at the surface ($r = R$) of the star [Unno et al., 1989, chapter 14].

The equations and boundary conditions have non-trivial solutions only for specific values of the frequency ω, which is therefore an eigenvalue of the problem. We call each solution, corresponding to both the eigenfrequency $\omega_{n\ell}$ and the eigenfunction (the run of the perturbations ξ, p', etc. with r) a mode of oscillation. The *radial order* n corresponds essentially to the number of zeros in the radial direction in the eigenfunctions.

Due to their homogeneity, Eqs. (2.3) only determine the solution up to a constant factor; the amplitude of the perturbations is not determined in the linear approximation.

2.2 Asymptotic analysis

Analytical solutions to the full set of equations of adiabatic oscillations exist only in very particular cases (like the case of an isothermal atmosphere or a non-gravitating sphere [Aerts et al., 2010]). The full fourth order system can be solved numerically, but some insight might be obtained by making a simplifying assumption, the so called *Cowling approximation*. This will allow us to write a general but approximate second-order differential equation for ξ, define the propagation region of p modes and simplify the subsequent asymptotic analysis needed to construct diagnostic tools.

Cowling approximation

Together with the system of three equations mentioned above, the perturbation to the gravitational potential Φ' also satisfies the perturbed Poisson equation

$$\nabla^2\Phi' = 4\pi G\rho' \tag{2.4}$$

or in separated form

$$\frac{1}{r^2}\frac{d}{dr}\left(r^2\frac{d\Phi'}{dr}\right) - \frac{\ell(\ell+1)}{r^2}\Phi' = 4\pi G\rho' \tag{2.5}$$

which has the integral solution (can be verified by substitution in 2.5)

$$\Phi'(r) = -\frac{4\pi G}{2\ell+1}\left[\frac{1}{r^{\ell+1}}\int_0^r \rho'\,(r')^{\ell+2}dr' + r^{\ell}\int_r^R \frac{\rho'}{(r')^{\ell-1}}dr'\right] \tag{2.6}$$

From Eq. (2.6) it follows that Φ' is small compared to ρ' in one of two cases: if ℓ is large or if the radial order $|n|$ is large [Cowling, 1941]. Under one or both of these circumstances, it is reasonable, and indeed accurate, to neglect the perturbation to the gravitational potential, Φ' [Christensen-Dalsgaard, 1991]. By doing that, the oscillation equations can be written in the form

$$\begin{aligned} \frac{d\xi}{dr} &= -\left(\frac{2}{r} - \frac{g}{c^2}\right)\xi - \left(1 - \frac{S_l^2}{w^2}\right)\frac{p'}{\rho c^2} \\ \frac{dp'}{dr} &= \frac{g}{c^2}p' + \left(w^2 - N^2\right)\rho\xi \end{aligned} \tag{2.7}$$

The two equations in Eq. (2.7) can be combined in a single second-order differential equation if we neglect the derivatives of g and r (basically, this means assuming that the oscillations vary more rapidly than g and r so that, locally, the problem is one of oscillations in a plane-parallel layer under constant gravity). The result is the equation [e. g. Deubner and Gough, 1984]

$$\frac{d^2X}{dr^2} + \frac{1}{c^2}\left[S_\ell^2\left(\frac{N^2}{\omega^2} - 1\right) + \omega^2 - \omega_c^2\right]X \quad = \quad 0 \tag{2.8}$$

for the quantity $X = c^2\rho^{1/2}\mathrm{div}\delta r$. Here we have introduced the acoustic cut-off frequency

$$\omega_c^2 = \frac{c^2}{4H^2}\left(1 - 2\frac{dH}{dr}\right)$$

where $H = -(d\ln\rho/dr)^{-1}$ is the density scale height. The main properties of the eigenfunctions that are solution of (2.8) are determined by the properties of

$$K \equiv \frac{1}{c^2}\left[S_\ell^2\left(\frac{N^2}{\omega^2} - 1\right) + \omega^2 - \omega_c^2\right]$$

In general, a mode is oscillatory in terms of r where $K > 0$ and decays exponentially (is *evanescent*) where $K < 0$. We usually say that a mode is trapped in the region where it shows oscillatory behavior, and its frequency will be predominantly determined by the structure of the star in that region.

Two types of waves that can be excited in a star are acoustic waves that use pressure as the driving mechanism (p modes), and gravity waves supported by the buoyancy of the gas (g modes). By a careful analysis of the quantity K, that depends on N^2 and S_ℓ, we can determine the regions inside the star where each type of mode is trapped.

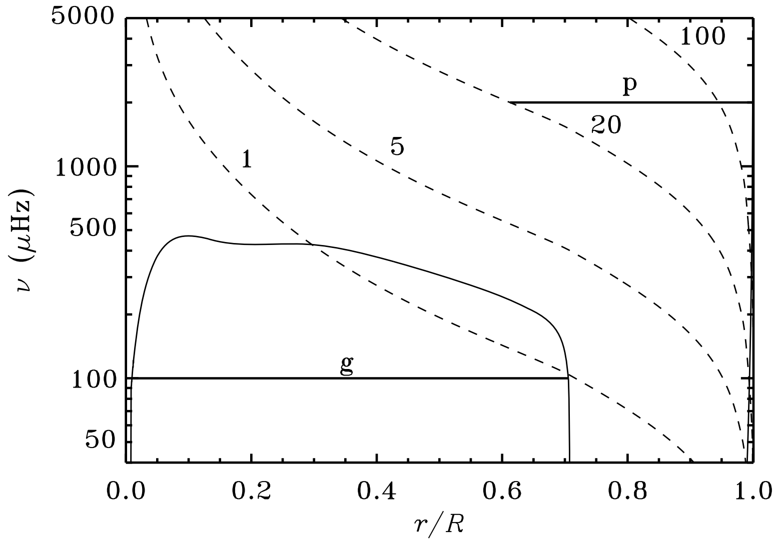

Fig. 2.1 - Brunt-Väisälä frequency N (solid line) and Lamb frequency S_ℓ (dashed lines, labeled by the values of ℓ), shown in terms of the corresponding cyclic frequencies, against fractional radius r/R for a model of the Sun. The horizontal lines indicate the trapping regions for a g mode with frequency $\nu = 100\mu$Hz, and for a p mode with degree 20 and $\nu = 2000\mu$Hz. From Aerts et al. [2010].

Typical regions where p and g modes are trapped are shown in Figure 2.1 for a model of the Sun.

By JWKB analysis† of the asymptotic equation (2.8), it is possible to show that the eigenfrequencies of low-degree p modes satisfy the relation (Gough [1993], see also Tassoul [1980, 1990])

$$\nu_{n\ell} = \frac{\omega_{n\ell}}{2\pi} \simeq \left(n + \frac{\ell}{2} + \frac{1}{4} + \alpha\right)\Delta\nu_0 - [A\ell(\ell+1) - \delta]\,\frac{\Delta\nu_0^2}{\nu_{n\ell}} \tag{2.9}$$

where

$$\begin{aligned}
\Delta\nu_0 &= \left(2\int_0^R \frac{dr}{c}\right)^{-1} \\
A &= \frac{1}{4\pi^2\Delta\nu_0}\left[\frac{c(R)}{R} - \int_0^R \frac{dc}{dr}\frac{dr}{r}\right]
\end{aligned}$$

and α and δ are quantities related to the near-surface region.

†Basically, the JWKB method assumes a solution of Eq. (2.8) that varies rapidly compared with equilibrium quantities, i. e., compared with $K(r)$. This solution is written in the form $X(r) \sim \exp[i\Psi(r)]$ where Ψ is rapidly varying. After substitution back into (2.8) the powers of $k_r = d\Psi/dr$ are equated and an approximate solution for $X(r)$ is obtained to the desired order. See Aerts et al. [2010, Chap. E.3] and also Gough [2007].

Neglecting the last second-order term, Eq. (2.9) predicts a uniform spacing between modes of the same angular degree ℓ and consecutive radial order (see Figure 2.2). This difference is known as the *large frequency separation*

$$\Delta\nu_{n\ell} = \nu_{n+1\,\ell} - \nu_{n\ell} \tag{2.10}$$

and is approximately equal to $\Delta\nu_0$ in a first approximation. Moreover, we can also predict a degeneracy between modes with the same parity (same value of $n + \ell/2$)

$$\nu_{n\,\ell} \simeq \nu_{n-1\,\ell+2} \tag{2.11}$$

Departure from the degeneracy in Eq. (2.11) is measured by the *small frequency separations*

$$d_{\ell,\ell+2} = \nu_{n\,\ell} - \nu_{n-1\,\ell+2} \tag{2.12}$$

which can be related to the second order term in (2.9) and shown to be

$$d_{\ell,\ell+2} \simeq -(4\ell+6)\,\frac{\Delta\nu_0}{4\pi^2\nu_{n\ell}}\int_0^R \frac{dc}{dr}\frac{dr}{r} \tag{2.13}$$

Another small separation that uses modes of degree $\ell = 0, 1$ can carry equivalent information

$$\begin{aligned} d_{\ell,\ell+1} &= \nu_{n\,\ell} - \frac{1}{2}\left(\nu_{n-1\,\ell+1} + \nu_{n\,\ell+1}\right) \\ &\simeq -(2\ell+2)\,\frac{\Delta\nu_0}{4\pi^2\nu_{n\,\ell}}\int_0^R \frac{dc}{dr}\frac{dr}{r} \end{aligned} \tag{2.14}$$

The above equations show the sensitivity of the small separations to the sound speed gradient near the core of the star which is itself very sensitive to the composition profile in that region. The small frequency separations thus present an important diagnostic of stellar evolution and stellar age.

One convenient way to illustrate schematically the frequency structure that results from Eq. (2.9) is to use the so-called *échelle diagram*[‡] where the frequency axis is cut into pieces of length $\Delta\nu_0$ which are stacked on top of each other. This yields points arranged in vertical lines corresponding to different values of ℓ, each separated by the appropriate small separation (Figure 2.3). It is clear from the figure that the observed frequencies show departures from the asymptotic behaviour, although the general structure is as

[‡]A commonly used citation when referring to this diagram is the work of Grec et al. [1983], although the word *échelle* (French for *ladder* or *scale*) is never mentioned in this work and its first use is indeed unknown to the author.

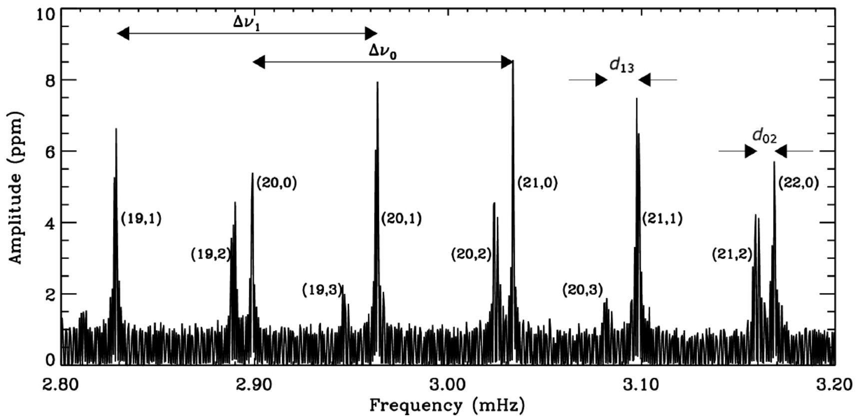

Fig. 2.2 - Amplitude spectra of solar oscillations measured by the VIRGO instrument on SOHO. A small portion of the solar oscillation spectrum is shown, as well as the large separations (identified only by the relevant ℓ subscript) and small separations d_{02} and d_{13}. Each frequency peak is labeled with the (n, ℓ) values of the oscillation mode. Adapted from [Catala, 2009]

expected. The curvature of the lines results from the structure near the solar surface and the combined effects of α and δ. Also, the small separations clearly vary with frequency.

2.3 Frequency combinations

In the discussion above I have already described the large and small separations: two combinations of the oscillation frequencies that are sensitive to different aspects of the stellar interior. It is possible to derive further relationships that will allow us to isolate specific regions of the star and extract information about them.

The predicted photometric amplitudes of the modes with degrees $\ell = 0, 1$ are considerably larger than those with $\ell = 2, 3$ [e. g. Aerts et al., 2010]. For some stars this may constitute a problem when calculating the small separations that need consecutive modes. Nevertheless, and particularly for solar-type stars, there has been a substantial increase in the number of modes detected. For the two stars that this work focuses on, a clear detection of $\ell = 3$ modes has been made in the *Kepler* data, although the inherent uncertainties are still high (see Section 4). We are thus interested in the diagnostic potential of frequency combinations that may involve $\ell = 0, 1, 2, 3$ modes.

2.3.1 *Signatures of the interior regions*

One useful diagnostic is the ratio of small to large separations, which is essentially independent of the structure of the outer layers of the star, as was shown by Roxburgh and Vorontsov [2003], Otí Floranes et al. [2005]. Different ratios can be constructed, such as

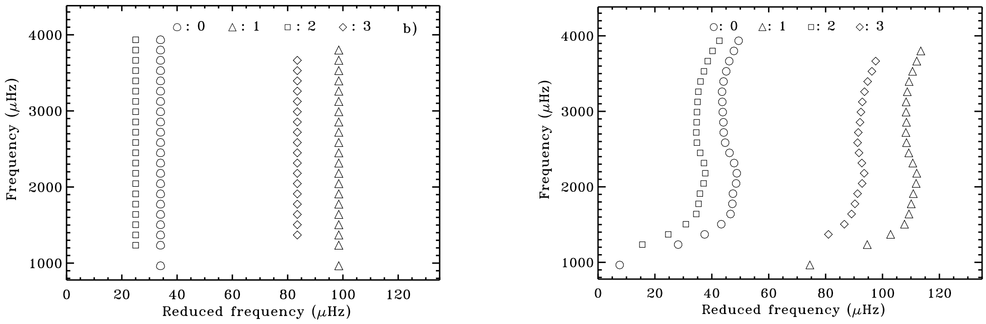

Fig. 2.3 - *Left:* Échelle diagram based on Eq. (2.9) with parameters chosen to match approximately the solar values. *Right:* Échelle diagram for observed solar frequencies obtained with the BiSON network [Chaplin et al., 2002]. Both diagrams are plotted with $\Delta\nu_0 = 135\,\mu$Hz. Circles, triangles, squares and diamonds are used for modes of degree $\ell = 0, 1, 2$ and 3. From Aerts et al. [2010].

$$
\begin{aligned}
r_{02}(n) &= \frac{d_{02}(n)}{\Delta_1(n)} = \frac{\nu_{n,0} - \nu_{n-1,2}}{\nu_{n,1} - \nu_{n-1,1}} \\
r_{13}(n) &= \frac{d_{13}(n)}{\Delta_0(n+1)} = \frac{\nu_{n,1} - \nu_{n-1,3}}{\nu_{n+1,0} - \nu_{n,0}} \\
r_{01}(n) &= \frac{d_{01}(n)}{\Delta_1(n)} = \frac{\nu_{n,0} - (\nu_{n-1,1} + \nu_{n,1})/2}{\nu_{n,1} - \nu_{n-1,1}} \\
r_{10}(n) &= \frac{d_{10}(n)}{\Delta_0(n+1)} = \frac{-\nu_{n,1} + (\nu_{n,0} + \nu_{n+1,0})/2}{\nu_{n+1,0} - \nu_{n,0}}
\end{aligned}
\tag{2.15}
$$

and used to probe the interior regions of the star. Another useful form for the ratios r_{01} and r_{10} uses five consecutive modes to achieve a smoother variation with frequency:

$$
\begin{aligned}
r^*_{01}(n) &= \frac{1}{8}\frac{\nu_{n-1,0} - 4\nu_{n-1,1} + 6\nu_{n,0} - 4\nu_{n,1} + \nu_{n+1,0}}{\nu_{n,1} - \nu_{n-1,1}} \\
r^*_{10}(n) &= -\frac{1}{8}\frac{\nu_{n-1,1} - 4\nu_{n,0} + 6\nu_{n,1} - 4\nu_{n+1,0} + \nu_{n+1,1}}{\nu_{n+1,0} - \nu_{n,0}}
\end{aligned}
\tag{2.16}
$$

Both the starred and the regular versions of r_{01} and r_{10} are usually considered together as a function of frequency in the quantity r_{010} as

$$
r_{010} = \{r_{01}(n), r_{10}(n), r_{01}(n+1), r_{10}(n+1), r_{01}(n+2), \ldots\} \tag{2.17}
$$

As an example, Figure 2.4 shows the small separations d_{02} and the ratios r_{02} for the different models of the Sun considered by Roxburgh and Vorontsov [2003], that differ

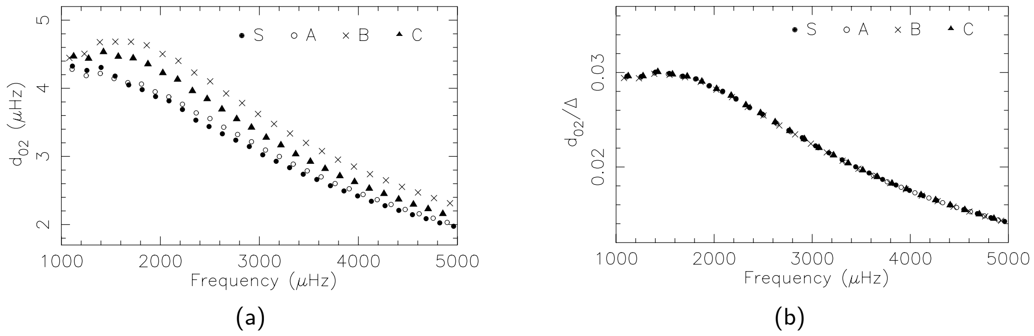

Fig. 2.4 - Small separations d_{02} (a) and ratios r_{02} (b) for four models of the Sun which differ only in the outer envelopes. Figures from Roxburgh & Vorontsov (2003).

only in their outer envelopes. It is clear that taking the ratio essentially suppresses the differences in the small separations of all four models.

The effect of small convective cores in the oscillation frequencies of solar-like stars has been studied by Cunha et al. [2007] who presented a diagnostic tool that isolates the signature of the core. This quantity can be written as

$$dr_{0213} = \frac{r_{02}(n)}{6} - \frac{r_{13}(n)}{10} \tag{2.18}$$

where the numerical coefficients in the denominators arise from the $4\ell + 6$ factor in (2.13).

All frequency combinations considered so far carry information about specific regions of the star. We will use them in Section 4.3 to try to improve the models of 16 Cyg A & B and compare them to observations.

2.3.2 *Signatures of sharp variation*

The large separations (2.10) can be regarded as a finite difference approximation for the first derivative of $\nu_{n,\ell}$ as a function of mode order n, for each angular degree ℓ. It then becomes clear that we can think of approximations to higher derivatives, and construct the *second differences*

$$\Delta_2\nu_{n,\ell} = \nu_{n-1,\ell} - 2\nu_{n,\ell} + \nu_{n+1,\ell} \tag{2.19}$$

as a central difference approximation to the second derivative, or the fourth differences

$$\Delta_4\nu_{n,\ell} = \nu_{n-2,\ell} - 4\nu_{n-1,\ell} + 6\nu_{n,\ell} - 4\nu_{n+1,\ell} + \nu_{n+2,\ell} \tag{2.20}$$

as an approximation to the fourth derivative, and so on.

The reason to consider such combinations lies in the dependence of the oscillation frequencies on localized sharp changes in the stratification, the so called acoustic glitches. A transition in the star's internal structure that is seismically abrupt (its radial extent is smaller than the typical wavelength of the eigenfunctions of low frequency modes) will cause a small departure from the asymptotic spacings. Each eigenfrequency will be affected by a shift, say $\delta\nu_n^{\text{glitch}}$ (the ℓ dependence is ignored), that is a periodic function of frequency and whose characteristics depend on the location and sharpness of the transition.

The shift is very small relative to the absolute value of the frequencies but can be enhanced by considering the second differences. To see why let us follow closely the derivation of Houdek and Gough [2007, henceforth HG07]. Assume an oscillatory signal of the form

$$\delta\nu_n^{\text{glitch}} = A_n \cos x_n \tag{2.21}$$

where A_n and x_n are functions of frequency. Expanding $A_{n\pm1}$ and $x_{n\pm1}$ in a Taylor series around A_n and x_n (considering the frequency ν_n a continuous function of mode order n) we find

$$\begin{aligned} x_{n\pm1} &\simeq x_n \pm \frac{d\nu_n}{dn}\frac{dx_n}{d\nu_n} \simeq x_n \pm \Delta\nu_0 \frac{dx_n}{d\nu_n} \equiv x_n \pm a \\ A_{n\pm1} &\simeq \left(1 \pm \frac{\nu_0}{A_n}\frac{dA_n}{d\nu_n} + \frac{\nu_0^2}{2A_n}\frac{d^2A_n}{d\nu_n^2}\right) A_n \equiv (1 \pm b + c)\, A_n \end{aligned} \tag{2.22}$$

where the derivatives of ν_n come from Eq. (2.9) at fixed ℓ and keeping only the leading term. From the definition of the second differences, Eq. (2.19), and writing each frequency as a sum of a smooth part ν_s and the shift $\delta\nu_n^{\text{glitch}}$, we obtain

$$\Delta_2\nu_{n,\ell} = \Delta_2\nu_s + F A_n \cos(x_n - \delta) \tag{2.23}$$

where

$$F = 2\left\{[1-(1+c)\cos a]^2 + b^2 \sin^2 a\right\}^{1/2} \tag{2.24}$$

and $\delta = \delta(a, b, c)$. For the Sun, and in the case of the glitch that is caused by the ionization of Helium near the solar surface, Houdek and Gough find $a \simeq 1.4$, $b \simeq -0.33$ and $c \simeq 0.04$ so that the oscillatory component is enhanced in the second differences by a factor of $F \simeq 1.7$. For the glitch present at the base of the solar convection zone, $a \simeq 4$, $b \simeq -0.10$ and $c \simeq 0.01$ so that in this case, $F \simeq 3.4$.

We see that in the second differences, the oscillatory component dominates over the smooth component (the latter is diminished since only second and higher order terms remain in $\Delta_2 \nu_s$) and may be easier to detect. In the next section I will study two methods to isolate the oscillatory signals both in the frequencies and in the second differences.

3

Measuring acoustic glitches

In Section 2.3.2 the second differences were introduced as probes of regions of rapid variation in the stellar interiors. The oscillatory signal produced by these regions is present in the oscillation frequencies and propagates to the second differences and also to other types of frequency combinations. In principle it can be detected both in the frequencies and in the second differences, with the difference that in the latter the smooth component that results from the run of the sound speed with radius (which would be present even in a hypothetical star with no glitches) is in part eliminated. The amplitude of the signal in the second differences is, thus, enhanced as was shown before.

In order to isolate the oscillatory signal, we need to know (or assume) its functional form and what are the parameters that describe it. In the following section I briefly discuss the derivation of the asymptotic expression for the signals (both at the base of the convection zone and at the helium ionization zone) and then present the actual expressions used to fit the signals. After that, two numerical methods used to isolate the signals are described and finally, in Section 3.4, the results for the Sun are presented as a validation of the codes.

3.1 Nature of the signal

In order to derive an expression for the variation in frequency caused by a discontinuity in the internal structure of the star we can use a proper approximation to the adiabatic oscillation equations either in differential or integral form. The former is simpler in the case of the base of the convection zone, but for the ionization region and to better approximate the frequency dependence of the amplitude of the signals a variational principle yields better results [Monteiro et al., 1994, Monteiro and Thompson, 2005].

Notwithstanding, if one considers the adiabatic oscillation equations in the Cowling approximation, which can be reduced to the Schrödinger-type equation [Brodsky and Vorontsov, 1993]

$$\frac{d^2}{d\tau^2}\zeta + \left[\omega^2 - V(\tau)\right]\zeta = 0 \tag{3.1}$$

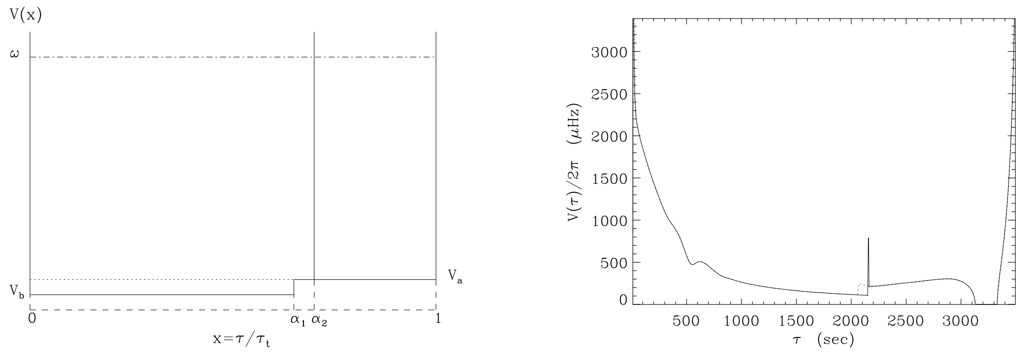

Fig. 3.1 - *Left:* Example of two types of perturbations in the acoustic potential as a function of normalized acoustic depth: a step at $\alpha_1\tau_t$ and a δ function at $\alpha_2\tau_t$. *Right:* Acoustic potential ($\ell = 0$) for two solar models with (dotted line) and without (solid line) taking into account convective overshoot. Adapted from Monteiro et al. [1994].

where τ is the acoustic depth, defined by

$$d\tau = -dr/c, \qquad \tau = 0 \text{ at } r = R \tag{3.2}$$

and ζ is the eigenfunction of the oscillation, we can illustrate the physical reason for the presence of the oscillatory signal. The acoustic potential V, whose explicit form will be given later, is a function of τ only that is defined by the internal structure of the star and contains terms in the first and second derivatives of the sound speed. A discontinuity in the first derivative of the sound speed produces a δ-function in V and a discontinuity in the second derivative gives rise to a step function in V.

Now consider two potentials for which we can obtain an exact solution and that illustrate both types of singularities (left panel of Fig 3.1)

$$V_1(\tau) = \begin{cases} V_b & \text{for} \quad 0 \le \tau < \alpha_1\tau \\ V_a & \text{for} \quad \alpha_1\tau \le \tau < \tau_t \end{cases} \tag{3.3}$$

and

$$V_2(\tau) = V_a + A_\delta\delta(\tau - \alpha_2\tau_t) \tag{3.4}$$

where τ_t is the total acoustic radius of the star. Expanding the solutions of equation (3.1) with the two potentials V_1 and V_2 to first order in the small quantity $\delta\omega = \omega - \omega_0$, that represents the frequency shift, and $\delta V^2 = V_a^2 - V_b^2$ that represents the structure variation in the first case, we obtain the periodic component of $\delta\omega$ as

$$\delta\omega_1 \sim \frac{\delta V^2}{4\tau_t\omega_0^2}\sin[2\Lambda_0(\alpha_1\tau_t)] \tag{3.5}$$

and

$$\delta\omega_2 \sim \frac{A_\delta}{2\tau_t\omega_0}\cos[2\Lambda_0(\alpha_2\tau_t)] \tag{3.6}$$

for the two potentials respectively, where

$$\Lambda_0(\tau) = \int_0^\tau (\omega_0^2 - V_a^2)^{\frac{1}{2}} d\tau. \tag{3.7}$$

These very simple examples already provide important insights about the frequency dependence of the amplitude of the signal and indeed do not differ much from the results obtained for a star, in which case the toy potentials will be replaced by a more complicated function that depends on the interior of the star and can be determined numerically from models (see Figure 3.1).

The explicit dependence of the acoustic potential on the sound speed and its derivatives can be written as [Vorontsov and Zharkov, 1989, Roxburgh and Vorontsov, 1994]

$$\begin{aligned} V^2 =& N^2 + \frac{c^2}{4}\left(\frac{2}{r}+\frac{N^2}{g}-\frac{g}{c^2}-\frac{1}{2c^2}\frac{dc^2}{dr}\right)^2 \\ &-\frac{c}{2}\frac{d}{dr}\left[c\left(\frac{2}{r}+\frac{N^2}{g}-\frac{g}{c^2}-\frac{1}{2c^2}\frac{dc^2}{dr}\right)\right]-4\pi G\rho\,, \end{aligned} \tag{3.8}$$

At the base of the convection zone, g, c^2 and ρ are continuous but both dc^2/dr and d^2c^2/dr^2 are discontinuous. Therefore, V can be decomposed as

$$V(\tau) = V_0(\tau) + A_H H(\tau-\tau_b) + A_\delta\,\frac{1}{c}\,\delta(\tau-\tau_b), \tag{3.9}$$

where $V_0(\tau)$ is a smooth function of τ and $\tau = \tau_b$ is the acoustic location of the base of the convection zone (H is the Heaviside function). Note that (3.9) has terms that are of the form (3.3) and (3.4) so that the base of the convection zone will give rise to a periodic effect on the frequencies that is a combination of both (3.5) and (3.6).

A similar analysis can be performed for the second Helium ionization region which induces a local change to the first adiabatic exponent Γ_1. The potential can be reduced to the form [Marchenkov and Vorontsov, 1991]

$$V^2 \approx \frac{g^2}{16\,c^2}\left[(1+\Gamma_1)(3-\Gamma_1)+2(1+\Gamma_1)\frac{d\,\Gamma_1}{d\ln p}-\left(\frac{d\,\Gamma_1}{d\ln p}\right)^2+4\,\Gamma_1\frac{d^2\,\Gamma_1}{d(\ln p)^2}\right], \tag{3.10}$$

but now it is no longer feasible to consider discontinuities in the first and second derivatives of Γ_1. Instead, ionization causes a "bump" or a depression in the adiabatic exponent that extends through approximately 300 s.

To model this signature we follow Monteiro and Thompson [2005] and consider a bump of width β in acoustic depth and relative height δ_d. It can be shown that, relative to a smooth model (one that has no He ionization), the frequencies will be affected by a periodic component of the form

$$\delta\omega \sim A(\omega)\cos(2\omega\tau_d^* + \phi) \tag{3.11}$$

The parameter τ_d (see Figure 3.2) corresponds to the acoustic depth of the middle of the bump, but the period of the signal that will be present on the frequencies will also contain a contribution from the near-surface layers, meaning that what we will be able to measure will not necessarily be a good estimate of this location[†]. Also there is no trivial relation between the true location τ_d and the measured period of the signal τ_d^*, although a difference of about $200\,$s between the two is expected [Monteiro and Thompson, 2005].

Although without extensive derivations (the interested reader is referred to the works of, e. g., Monteiro et al. [1994] and HG07) we have demonstrated that a periodic signal in the frequencies appears as a result of sharp changes in the acoustic stratification of stars.

3.2 Complete expressions

We have demonstrated the reasons for periodic signals to be present in the oscillation frequencies due to the effect of the BCZ and the HeIIZ. Here we describe the exact form of the signals that will be fitted to the observed frequencies and also document the notation used below. From now on we shall write all expressions in terms of the cyclic frequency $\nu = \omega/2\pi$.

Since only low degree data is available, all dependencies of the signals on ℓ are ignored. A reference frequency ν_r will be used to normalize the amplitudes. This value does not interfere in the fit but to compare the signal in different stars we need to use the same

[†]This will also affect the location of the base of the convection zone

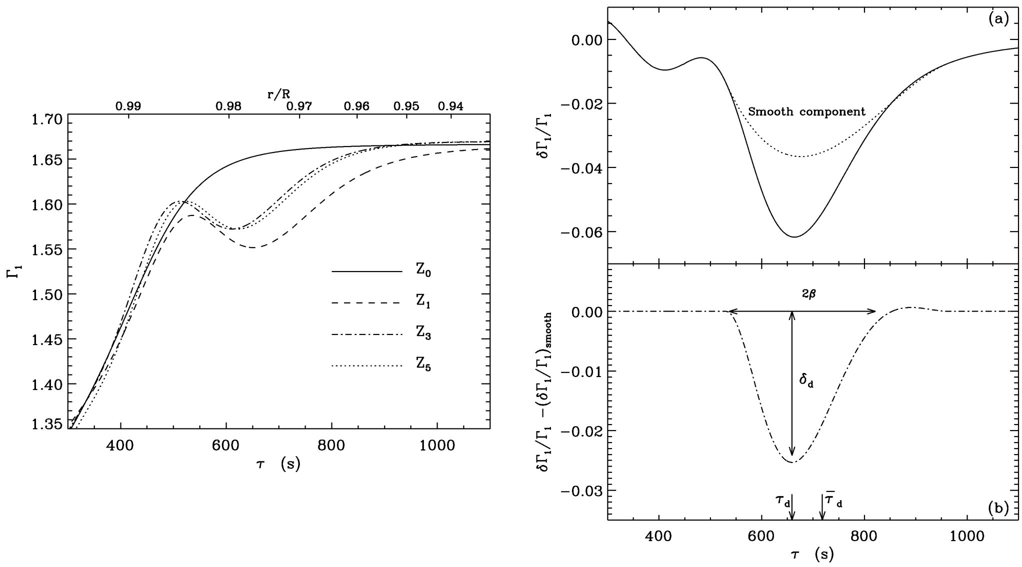

Fig. 3.2 - *Left:* The adiabatic exponent Γ_1 for different solar models. In model Z_0 the second ionization of Helium has been suppressed while the other three models have different equations of state. *Right:* a) The differences in Γ_1 between two models with and without the second ionization of Helium (Z_0 and Z_1 respectively) plotted as a function of acoustic depth τ. b) The change in Γ_1 relative to a smooth reference structure. The parameters that define the signal present in the frequencies are represented schematically (see text). Adapted from Monteiro and Thompson [2005].

reference frequency. All amplitude values referred below will be amplitudes of the signal, or of each component, evaluated at ν_r (we have used $\nu_r = 2000\,\mu$Hz).

Let us consider the observed values of the frequencies to be given by

$$\nu = \nu_s + \delta\nu_{\text{HeIIZ}} + \delta\nu_{\text{BCZ}} \tag{3.12}$$

where ν_s is the smooth component that needs to be removed when fitting the signals. The expression from the HeIIZ component to be used is the one considered in Monteiro and Thompson [2005], namely

$$\delta\nu_{\text{HeIIZ}} = A_{\text{HeIIZ}} \left(\frac{\nu_r}{\nu}\right) \sin^2(2\pi\beta_{\text{HeIIZ}}\nu) \cos(4\pi\tau_{\text{HeIIZ}}\nu + 2\phi_{\text{HeIIZ}}) \tag{3.13}$$

which has the four free parameters, A_{HeIIZ}, β_{HeIIZ}, τ_{HeIIZ} and ϕ_{HeIIZ} corresponding, respectively, to amplitude of the signal, acoustic width, acoustic depth (see Fig 3.2) and phase. For the base of the convection zone we consider the expression derived in Monteiro et al. [1994]

$$\delta\nu_{\text{BCZ}} = A_{\text{BCZ}} \left(\frac{\nu_r}{\nu}\right)^2 \cos(4\pi\tau_{\text{BCZ}}\nu + 2\phi_{\text{BCZ}}) \tag{3.14}$$

with free parameters A_{BCZ}, τ_{BCZ} and ϕ_{BCZ} corresponding to amplitude, acoustic depth and phase of the BCZ signal.

To obtain the final expression to fit the frequencies we need in addition to specify the smooth component ν_s in (3.12) but the functional form of this component is unknown. For now we will leave it unspecified but in Section 3.3 the method used to remove this slowly varying trend will be described. The final function to fit to the frequencies is then

$$\begin{aligned} \nu \simeq \nu_s &+ \\ &+ A_{\text{BCZ}} \left(\frac{\nu_r}{\nu}\right)^2 \cos(4\pi\tau_{\text{BCZ}}\nu + 2\phi_{\text{BCZ}}) + \\ &+ A_{\text{HeIIZ}} \left(\frac{\nu_r}{\nu}\right) \sin^2(2\pi\beta_{\text{HeIIZ}}\nu) \cos(4\pi\tau_{\text{HeIIZ}}\nu + 2\phi_{\text{HeIIZ}}) \end{aligned} \tag{3.15}$$

In order to derive the expressions for the second differences, the same analysis of Section 2.3.2 can be carried out, already assuming the functional form (3.15) in the frequencies. Guided by the frequency dependence of the asymptotic relation (2.9), we can approximate the smooth component that is left in the second differences by a polynomial (up to third-degree) in ν^{-1}. However, for the range of frequencies available for 16 Cyg A and B we find that a simpler constant term is more suitable.

The final functional form that will be fitted to the observed second differences is based on the one used in Mazumdar et al. [2012], namely

$$\begin{aligned} \Delta_2\nu = \sum_{k=0}^{3} c_k \nu^{-k} &+ \\ &+ \left(A^*_{\text{BCZ}}/\nu^2\right) \sin\left(4\pi\nu\tau_{\text{BCZ}} + 2\phi_{\text{BCZ}}\right) + \\ &+ \left[A^*_{\text{HeIIZ}}\, \nu \, \exp\left(-\beta^*_{\text{HeIIZ}}\, \nu^2\right)\right] \sin\left(4\pi\nu\tau_{\text{HeIIZ}} + 2\phi_{\text{HeIIZ}}\right) \end{aligned} \tag{3.16}$$

with seven free[‡] parameters A^*_{BCZ}, τ_{BCZ}, ϕ_{BCZ}, A^*_{HeIIZ}, β^*_{HeIIZ}, τ_{HeIIZ} and ϕ_{HeIIZ}.

3.2.1 *Expressions from Houdek & Gough*

It is worth mentioning the latest results in the development of more elaborate expressions for the signals. Houdek and Gough [2007] performed an asymptotic analysis of the effects of the helium ionization region and the base of the convection zone on the frequencies. They derived an expression that in principle represents the second differences more faithfully than the expressions we are using, because their representation of the He II glitch in Γ_1 and of the stratification immediately beneath the convection zone is more realistic.

[‡]The parameters of the polynomial smooth component (either c_{0-3} or just c_0) are still free parameters but they are not included in the nonlinear fit, as will be discussed in the next section.

The more complete expressions for the glitches come with the price of having to assume many intermediate parameters in the derivation to have their solar (or solar calibrated) values. While correct and advantageous in the case of the Sun, many of these parameters do not have observable values in other stars.

We have carried out tests trying to fit the more realistic expressions [HG07, their Eq. 22] to the second differences of the Sun and of 16 Cyg A & B. For the Sun, the results were only marginally better than when fitting Eq. (3.16). For the 16 Cyg stars we were not able to find good fits. Thus, and also supported by the fact that many parameters would have to be set to solar values, we have not considered further these expressions. The added complexity of the functional forms does not yet seem beneficial when applied to other stars, at least until extremely precise data (comparable to the solar data) is available. Also, while not the exact form prescribed by [HG07], Eq. (3.16) does contain the essential terms.

3.3 Methods to isolate the signals

This section is devoted to the description of two different numerical methods to isolate and determine the parameters of the signals given by Eq. (3.15) in the frequencies or Eq. (3.16) in the second differences.

The first method that we consider (henceforth labeled Method 1) was presented in Monteiro et al. [1994] and subsequently used to study the convective overshoot properties and the helium abundance of the Sun [Monteiro et al., 2000, Monteiro and Thompson, 2005]. It has also been applied to other solar-type stars [Mazumdar et al., 2012].

The idea is to extract the signal from the oscillation frequencies directly, by fitting a smooth function of mode order n to the points $\nu_{n,\ell}$ in order to remove the slowly varying trend. This is done separately for each degree ℓ, by fitting the polynomial

$$P_\ell(n) = \sum_{k=1}^{N_\ell} a_k^{(\ell)} n^{k-1} \tag{3.17}$$

to the N_ℓ frequencies using a least squares fit with third derivative smoothing. The residuals are then fitted (simultaneously for all degrees) with the expression for the signal. By iterating this procedure, the smooth function will remove variations of $\nu_{n,\ell}$ with scales much longer than the characteristic scale of the signal without affecting it.

The third derivative smoothing procedure depends on a parameter λ that basically determines how close the polynomial P_ℓ interpolates the points or, said in another way, how smooth it is. In the original Method 1 there is an iteration over this parameter that tries to achieve the smoothest possible function that still does not interfere with the signals we are trying to extract (the reader is referred to Monteiro et al. [1994] for all the details).

The fact that Method 1 makes use of all the data available (does not require frequencies of consecutive orders to construct combinations) and that it does not assume a specific functional form for the smooth component are its main advantages. It can, however, in its current implementation, be less robust (more dependent on starting conditions) than other methods. This is because it uses a local minimization algorithm, meaning that the initial conditions must be close to the true properties of the signal that is to be extracted.

A second method (henceforth, Method 2) uses the second frequency differences and fits the functional form (3.16) to the observed points $\Delta_2\nu_{n,\ell}$. It was discussed before that the amplitudes of the signals are enhanced relative to the smooth component when we take the second differences which means that the signals might be more easily extracted. The functional form of the smooth component is still not known *a priori* but can be approximated by a polynomial function of frequency.

Because it uses the second differences, Method 2 needs three consecutive modes of the same degree for each point. In stars where only a small number of modes are observed we can reach the limiting case of not having enough points to fit (or having few more points than free parameters). In the case of the available data for 16 Cygni though, there are many observed modes and this is not a severe problem.

Both Method 1 and 2 have been compared with each other and with other methods to isolate the signals [Mazumdar et al., 2012] and shown to give consistent results. In the next sections we describe our own implementations and some improvements to both methods which we then use to study the acoustic glitches of 16 Cyg A & B.

3.3.1 *Improving Method 1*

In previous works, Method 1 has been used to isolate the contributions from the base of the convection zone and from the helium ionization separately. This is in part due to the difficulty in choosing a scale for the smooth function that does not affect the characteristics of the signals when both are considered together, but mostly is because of convergence problems.

The value of the smoothing parameter λ determines the period of the signal that is to be isolated. Depending on the choice of this parameter, we either ensure that the signature associated with helium ionization is removed (with smaller values of λ) or allow it to dominate the least-squares fit (larger λ). In the latter case, the signature from the base of the convection zone is still retained, although it may be more difficult to isolate.

We have tried to improve Method 1 in two complementary ways: using a global minimization algorithm for the least-squares fit that provides robustness and independence of initial conditions (see Section 3.3.3) and fitting both signals from the BCZ and the HeIIZ together.

From tests of the parameter dependence on λ, we are able to identify a "plateau" where both the parameters of the fit and the χ^2 remain approximately unchanged in a range of values of λ. We then set this parameter to an intermediate value inside this range.

It is important to understand why the original iteration in λ was removed. A value of $\lambda = 0$ means the interpolating polynomial will pass through all points, effectively without smoothing. Then, if λ is included in the fit as a free parameter, the best solution will always converge to a value very close to zero, artificially making the smooth function explain every variation in the data. One possible solution would be to constrain the value of λ by, for example, penalizing the fit when the HeIIZ and BCZ signal amplitudes approach zero. Although this is feasible and worthy of additional studies, we have not tried to implement it, in part due to our inability to specify a coherent and justified penalty.

As will be shown in Chapter 4, the improved Method 1 is already quite robust, even with the arbitrariness of the setting of λ. This aspect of the fit is a shortcoming but is the price to pay for not assuming a functional form for the smooth contribution. The values used in the fits of 16 Cyg A and B were $\lambda_A = 10^{-4}$ and $\lambda_B = 5 \times 10^{-4}$ for the two components respectively.

3.3.2 *Implementation of Method 2*

The numerical implementation of Method 2 may seem simpler, but it is important to mention some of its subtleties and to document clearly our treatment.

The fit of the smooth component is carried out first and only once, so that either the constant term c_0 or the third degree polynomial is first subtracted from the data, leaving only seven free parameters describing the properties of both signals. The choice of the degree of the polynomial depends on the range of second differences available, although it will always be rather arbitrary. In the study of 16 Cygni we have only considered the constant term, while for the Sun we used the third degree polynomial, because of the larger range in frequencies. After removing the smooth component from the data, a non-linear least squares regression is performed by minimizing the usual χ^2 quantity (our objective function) with the same global minimization algorithm used in the frequencies (see Section 3.3.3).

The covariance term in the χ^2 (which should be present because of correlations between consecutive values of $\Delta_2\nu_{n,\ell}$) has not been considered as it will not affect the location of the minimum in the parameter space but only the numerical value of the χ^2 [e. g. Dodelson and Schneider, 2013]. Since we estimate the errors in the fitted parameters by performing Monte Carlo simulations (and do not linearise in any way the objective function about the minimum) our error estimates implicitly take into account the correlations.

It is customary to consider in the fit only frequencies with errors smaller than a specific value and/or actually remove one or more outliers. This practice is not ideal and we do not follow it. Instead, we make our fit (more) robust against discrepant values by performing a Iteratively Reweighted Least Squares regression [e. g. Street et al., 1988]. In this process, values that deviate substantially from an initial fitted curve are given less weight in a subsequent fit, and this is iterated until convergence (small relative variation of the parameters of the fit)[§]. More explicitly, we use the following algorithm:

1. Compute the inverse variance of the observations $w_{n,\ell} = 1/\sigma^2_{n,\ell}$ where $\sigma_{n,\ell}$ are the quoted uncertainties for the $\nu_{n,\ell}$ mode.
2. Compute the least-squares solution weighted by $w_{n,\ell}$.
3. Compute $\chi^2_{n,\ell} = (\Delta_2\nu_{n,\ell} - \Delta_2\nu)^2/\sigma^2_{n,\ell}$, where $\Delta_2\nu$ if the fitting function given by (3.16) and $\Delta_2\nu_{n,\ell}$ the observed value of the second difference.
4. Update the weights $w_{n,\ell} = Q/[\sigma^2_{n,\ell}\,(\chi^2_{n,\ell} + Q)]$ for some value of Q .
5. Go to step 2 and iterate to convergence.

The choice of Q sets the maximum effect an outlier can have on the fit. For an extreme outlier ($\chi^2_{n,\ell} \gg Q$), the effect of that point will be down-weighted by the factor $Q/\chi^2_{n,\ell}$. For points that are well fit by the model, the weight is $1/\sigma^2_{n,\ell}$ as in standard weighted least squares. A value of $Q = 4$ seems to work well in the context of this problem. By using this procedure, all the available second differences enter in the fit in a robust way.

3.3.3 *Global minimization*

The global minimization algorithm used here was the PIKAIA implementation of the genetic algorithm [Charbonneau, 1995]. A genetic algorithm is an heuristic search technique that incorporates the biological notion of evolution by means of natural selection. It

[§]Note that the parameter c_0 is determined before the actual fit when we consider a constant smooth component. In order to extend the robustness of the process to this parameter, we consider the median value of the second differences instead of the mean, which would be the least squares solution of fitting a constant.

can be used to perform numerical optimization on problems characterized by ill-behaved search spaces and a relatively large number of free parameters.

The two main advantages of using a genetic algorithm in this case are: no derivatives of the goodness of fit function with respect to model parameters need to be computed; no starting guesses need to be provided. In principle, and given enough time, the algorithm will always converge to the global optimal solution, the one with the smallest residuals.

From a more technical point of view, the behavior of the genetic algorithm was set to include one-point crossover and creep mutation operators, as well as fitness-based adjustment of the mutation rate [see Charbonneau, 2002]. In all fits, a population containing 50 individuals is evolved for a number of generations that can vary between 5000 and 7000. These options were tuned to offer a trade off between execution speed and convergence for our particular problem.

3.3.4 *Monte Carlo simulations*

After performing the fits with Methods 1 and 2 we try to estimate the errors in the signal parameters by measuring the impact of the observational uncertainties. Monte Carlo realizations of the data are produced by affecting the frequencies (note, not the second differences, in Method 2) with a random error, sampled from a normal distribution with standard deviation equal to the uncertainty quoted for the frequency. Each set of new frequencies is then fit in the same way as the original data.

As we will see in Section 4.4, the mean and median values of the resulting distributions of the parameters are very close, and the distributions are approximately normal in most cases, so we quote their standard deviation as the 1σ error in the corresponding parameter.

3.4 Code validation - signal in solar frequencies

It is important to validate the implementations of Methods 1 and 2 before applying them to 16 Cygni. To that end, we use low-degree solar frequencies, obtained from the BISON network [Broomhall et al., 2009, cf. Table 1] and compare with results of previous works. The data used here correspond to a set of 79 modes with $\ell = 0 - 3$ and with a mean uncertainty of $0.032\,\mu Hz$.

Starting with the signal in the frequencies, and for comparison with Monteiro et al. [1994] and Monteiro and Thompson [2005], we set $\lambda = 10^{-6}$ which corresponds to the value used to fit the Helium component (remember that each component was fitted

Table 3.1 - Comparison of acoustic locations in the Sun.

Sun	This work		Previous works	
	$\delta\nu$	$\Delta_2\nu$	$\delta\nu$ [a]	$\Delta_2\nu$
τ_{BCZ} (s)	2270	2303	2337	2273
τ_{HeIIZ} (s)	648	728	649	707

[a] Fits to 197 modes with $5 \leq \ell \leq 20$

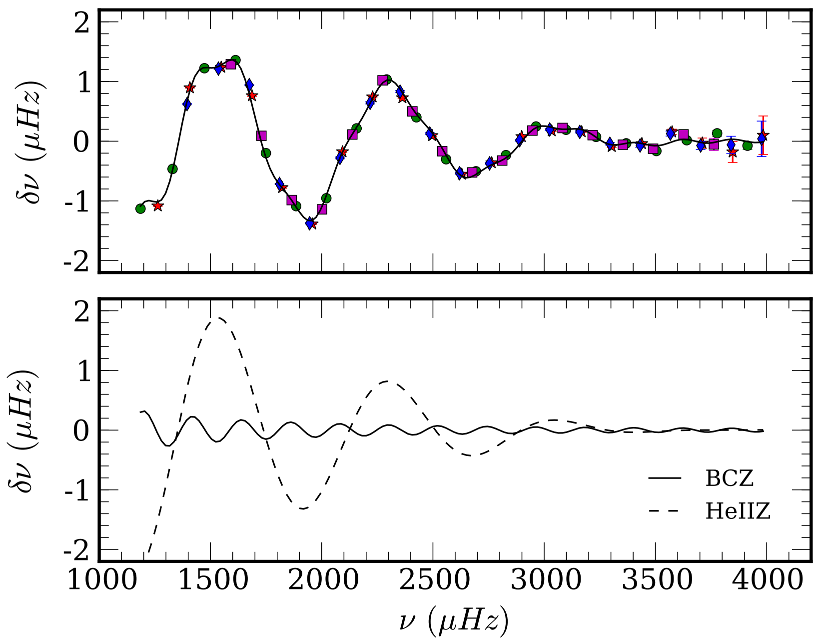

Fig. 3.3 - *Top:* Fit of Eq. (3.15) to the solar frequencies using the improved Method 1. The color and symbol code is as stated in Page vii. *Bottom:* Individual components from the BCZ (solid line) and the HeIIZ (dashed line).

separately in previous works). The results for the locations of the glitches (τ_{HeIIZ} and τ_{BCZ}) are shown in Table 3.1 and the fit itself is in Figure 3.3.

Table 3.1 shows also the results in the second differences from the fit using Method 2. These are to be compared to the results from HG07 obtained by fitting a slightly more elaborate form of the signal expression to GOLF and BISON data. Our fit is shown in Figure 3.4, together with the individual signal components (these should be compared to Figure 12 from HG07).

In the solar case we are not able to remove the smooth component using only a constant term, because of the bigger range in frequencies (almost $3000\,\mu Hz$). The third degree polynomial is used but it does not interfere with the HeIIZ component.

As a validation exercise, these results prove to be successful. We obtain good fits both to the solar frequencies and second differences and the signal parameters are close to those mentioned in the literature. Note that a perfect agreement is not to be expected

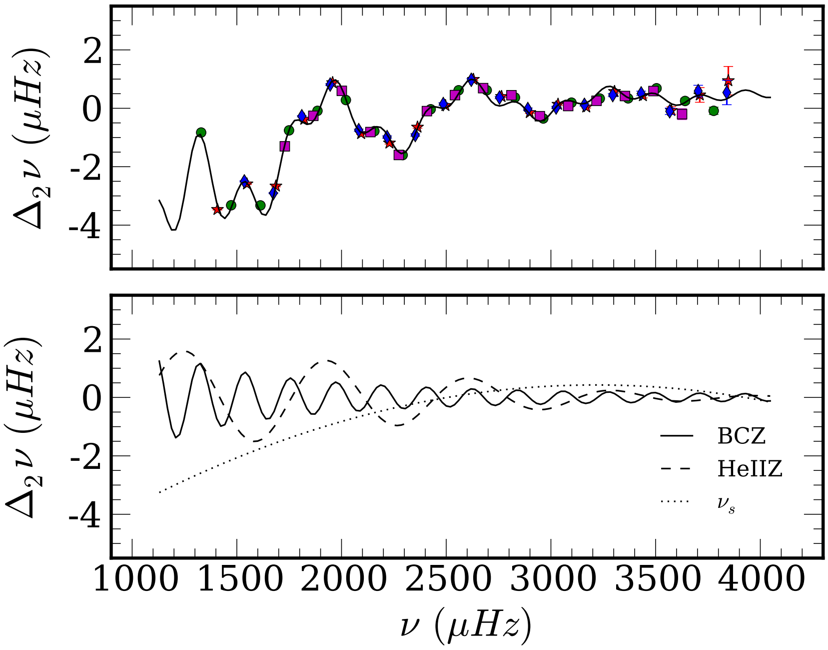

Fig. 3.4 - *Top:* Fit of Eq. (3.16) to the solar frequencies using our implementation of Method 2. The color code is the same as in Fig (3.3) *Bottom:* Individual components from the BCZ (solid line) and the HeIIZ (dashed line) as well as the third degree polynomial smooth component (dotted line).

since different frequency sets, different signal expressions and overall different methods were used.

3.5 Amplitude magnification

As was stated before, one of the reasons to consider the second differences and attempt the extraction of the signals in this quantity is the increased signal amplitudes. In fact, we should be more specific and say increased signal amplitudes *relative to the smooth component*, because it is the smooth component (on top of which both signals are superposed) that is diminished when taking the second differences.

If, and only if, both extraction methods effectively removed the same smooth function, we would expect the resulting amplitudes to be amplified by factors close to those derived in Section 2.3.2, approximately 3 times for the BCZ amplitude and 1.5 times for the HeIIZ amplitude (though note that those values were derived for the Sun). To test this prediction, both the BCZ and HeIIZ signals were extracted, using both Methods, from frequencies of representative models of 16 Cyg A and B. The amplitudes of each signal, at a given reference frequency, were then compared between the two Methods.

The results are shown in Figure 3.5. The dashed lines labeled '1:1' represent equal fitted amplitudes in both Methods. For the case of the BCZ signal, in both stars, there is indeed an amplitude amplification by a factor of about 3. For the HeIIZ signal this is not the case and the two Methods detect approximately the same amplitudes.

Assuming the theoretical predictions from Section 2.3.2 to be valid for the 16 Cyg binary as they are for the Sun, our results suggest that taking the second differences of the smooth function that is removed by Method 1 will not result in the exact constant term that is removed in Method 2.

To draw further conclusions from these results, we still need to discuss the error amplification involved in taking the second differences. Houdek and Gough [2007] presented an analysis regarding the relative signal error magnification for differences of various orders (frequencies, large separations, second differences, etc.). They show that one measure of the signal-to-noise ratio is higher in the frequencies for the case of the Helium ionization region, while it is higher in the second differences for the base of the convection zone. This means that the expected amplitude magnification of the HeIIZ signal is more than offset by the error magnification when taking successive differences. On the contrary, for the BCZ signal, the second differences seem to be the better diagnostic.

Our conclusion from the results of Figure 3.5, is that with the current implementations of methods 1 and 2 there seems to be no advantage in using the second differences to detect the HeIIZ signal because there is no clear amplitude magnification. For the BCZ signal we do obtain a magnification around the theoretically expected value but, as we will see in the following Chapter, the increased errors in the second differences result also in increased errors for the signal parameters.

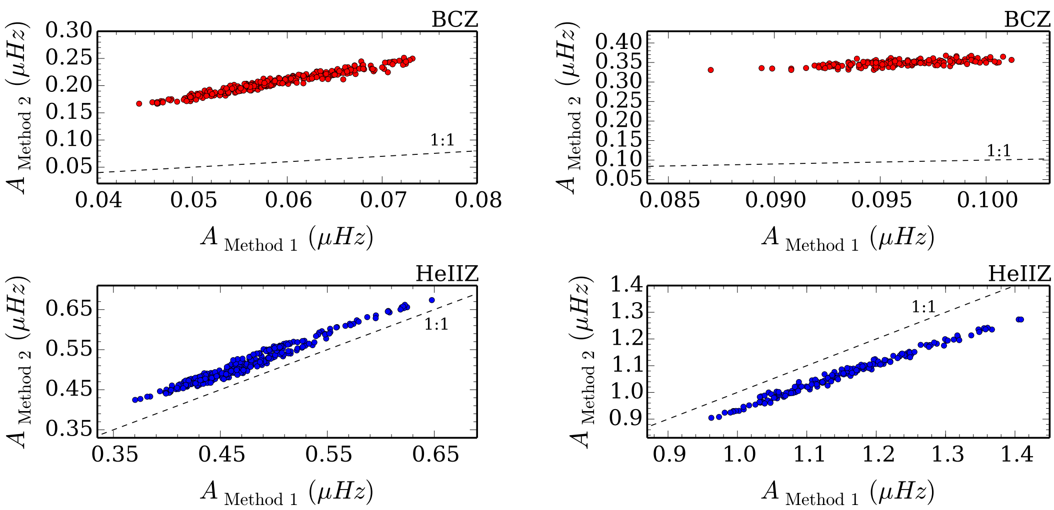

Fig. 3.5 - Amplitudes of the BCZ and HeIIZ signals obtained with Method 2 versus those obtained with Method 1 for 16 Cyg A (left) and B (right) using frequencies of representative models. The dashed line represents a one-to-one relation.

4

The solar-type stars 16 Cyg A & B

This chapter presents the analysis of the asteroseismic data of 16 Cyg A & B. It focuses on the modeling of both stars using the MESA code and in the detection and characterization of features related to the acoustic glitches, exploring the methods discussed in Chapter 3.

A discussion of the basic properties of both stars and of the 16 Cygni system as a whole (Section 4.1) is followed by a description of the available data from the *Kepler* space telescope. The observed oscillation frequencies are listed and will be used in the following sections for the asteroseismic analysis of these two sources. Section 4.3 gives the results of the stellar modeling and Section 4.4 shows results regarding the acoustic glitches. Finally in Section 4.5 a preliminary calibration of the surface helium abundance using the glitch parameters is presented.

4.1 Stellar properties

The two stars 16 Cyg A ($\mathrm{HD}\,186408$) and B ($\mathrm{HD}\,186427$) are a common proper-motion pair of solar analogs with spectral types G1.5V and G3V, respectively [Schuler et al., 2011]. Global stellar parameters and abundances have been derived by Ramírez et al. [2009] and recently White et al. [2013] combined interferometric observations from CHARA with parallaxes from Hipparcos and spectrophotometric bolometric fluxes to derive additional constraints. Both stars are physically very similar. Some relevant properties of the stars are summarized in Table 4.1. Their observed position in the HR diagram is shown in Figure 4.1, together with model tracks from Marques et al. [2008]. Note that the chemical composition of the models in these tracks is neither calibrated to the Sun nor to 16 Cyg so that the only insight coming from Figure 4.1 is to expect 16 Cyg A & B to be more evolved than the Sun.

One important difference between the two components is the presence of a $1.5\ \mathrm{M_{Jup}}$ planet in an eccentric orbit ($e = 0.63$) around 16 Cyg B [Cochran et al., 1997]. An M dwarf binary companion of 16 Cyg A, with a separation of $\sim 3''$ was also detected [Turner et al., 2001, Patience et al., 2002], and later confirmed by Raghavan et al. [2006].

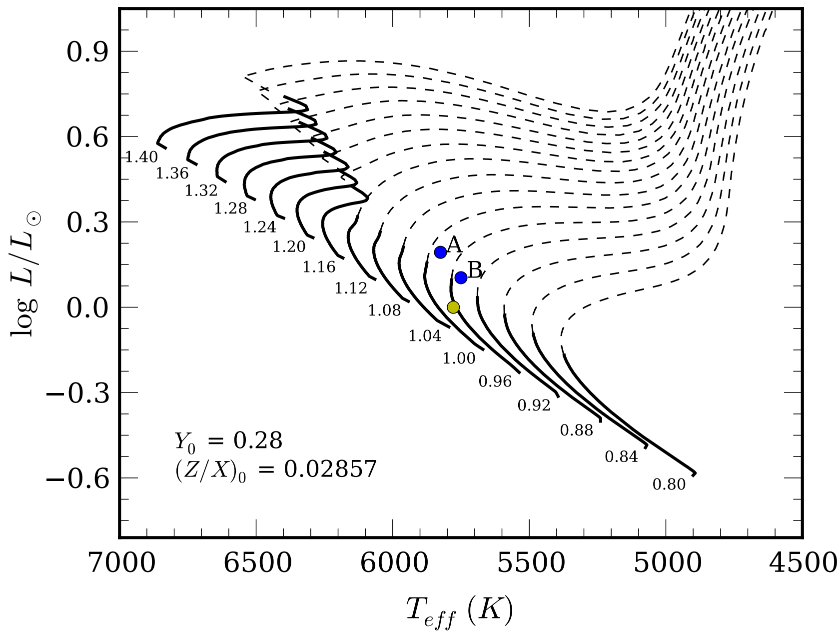

Fig. 4.1 - Position of the Sun (yellow circle) and 16 Cyg A and B (labeled blue circles) on the Hertzsprung-Russel diagram. Also shown are main-sequence (solid lines) and post main-sequence (dashed lines) evolutionary tracks for models of different masses, as indicated by the number near each track, from Marques et al. [2008] .

Despite being members of a hierarchical triple system, there are no dynamical constraints on the masses of the components A and B, due to an orbital period that is longer than 18000 years [Hauser and Marcy, 1999].

4.2 Kepler observations

Both 16 Cyg A and B have magnitudes around 6 mag. (see Table 4.1) and are among the brightest stars in the *Kepler* field of view. This fact has both the obvious advantage

Table 4.1 - Properties of 16 Cyg A & B.

	16 Cyg A	16 Cyg B	Sun
Distance [a] (pc)	21.1 ± 0.1	21.2 ± 0.1	-
m_V (mag)	5.96	6.20	-26.74
$T_{\rm eff}$ (K)	5839 ± 42 [b]	5809 ± 39 [b]	5777 [c]
$\log g$ [d]	4.33 ± 0.07	4.34 ± 0.07	4.438 [c]
[Fe/H] [d]	0.096 ± 0.026	0.052 ± 0.021	0.0

[a] van Leeuwen [2007]
[b] White et al. [2013]
[c] Cox [2001]
[d] Ramírez et al. [2009]

Table 4.2 - Global asteroseismic properties of 16 Cyg A and B.

	16 Cyg A	16 Cyg B
$\Delta\nu$ [a] (μHz)	103.5 ± 0.1	117.0 ± 0.1
$\Delta\nu$ [b] (μHz)	103.56 ± 0.14	116.89 ± 0.12
$\nu_{\max}$ [a] (μHz)	2201 ± 20	2552 ± 20

[a] White et al. [2013]
[b] Obtained from linear fit to radial modes

resulting from the increased brightness and the more technical downside of putting both stars above the saturation limit of the *Kepler* detectors. This problem was solved by applying custom masks, defined from Q$3^{\dagger}$ full frame images, that allow to capture the stars' flux using fewer pixels with no loss in photometric precision [Metcalfe et al., 2012].

The *Kepler* mission offers two modes of observation: long-cadence (LC) and short-cadence (SC), which differ in the sampling intervals ($29.42\,\mathrm{min}$ and $58.85\,\mathrm{s}$, respectively). As asteroseismology of solar-type stars requires the detection of oscillations with periods of $3-10$ minutes, the short cadence data is necessary. Both 16 Cyg A and B have been on the short cadence target list since Q7 (September 2010) with 2-year observations currently being prepared. The availability of longer data sets will increase the precision in the measured frequencies and maybe allow the detection of additional oscillation modes.

In this work we focus on a data set obtained with nine months of SC observations, in quarters Q$7-9$, with a total of 64 and 60 frequencies for both components respectively [e. g. García et al., 2011, Appourchaux et al., 2012]. These frequencies are shown in Table 4.3. Note the clear detection of $\ell = 3$ modes despite the fact that only at the mid-range in frequencies are the uncertainties comparable to those of other degree modes. In Figure 4.4 the same frequencies are represented in an échelle diagram.

The global properties of the oscillations can be derived directly from the light curve observations [e. g. Huber et al., 2009]. Values of the frequency of maximum power ν_{max} and the large separation $\Delta\nu$ for both stars are shown in Table 4.2. In the table, the value of the large separation obtained from a linear fit to the radial modes (from Eq. 2.9 one can see that the slope of this fit will approximate $\Delta\nu_0$ to first order) is also shown and agrees with the value obtained from the light curve.

†Every month, the *Kepler* space telescope must turn away from the monitored field, reorient toward the Earth for data download, and return to the field. The spacecraft also "rolls" every three months to allow for continuous illumination of its solar arrays. These three month periods define a quarter, each labeled as Qn. Despite this, the overall duty cycle of the observations is typically greater than 90%.

Table 4.3 - Observed oscillation frequencies for 16 Cyg A and B from nine months of *Kepler* data.

	16 Cyg A				16 Cyg B			
n	$\ell = 0$	$\ell = 1$	$\ell = 2$	$\ell = 3$	$\ell = 0$	$\ell = 1$	$\ell = 2$	$\ell = 3$
12	...	...	1490.01 ± 1.29	1530.85 ± 4.25	...	...	1686.36 ± 0.76	1735.55 ± 2.46
13	1495.02 ± 0.10	1541.92 ± 0.11	1591.50 ± 0.45	1629.82 ± 2.22	1695.10 ± 0.87	1749.14 ± 0.35	1804.75 ± 0.39	1855.06 ± 1.62
14	1598.57 ± 0.11	1644.90 ± 0.15	1693.88 ± 0.25	1736.54 ± 0.88	1812.31 ± 0.12	1866.42 ± 0.12	1921.23 ± 0.17	1969.76 ± 0.59
15	1700.87 ± 0.14	1747.06 ± 0.13	1795.87 ± 0.26	1836.69 ± 0.47	1928.89 ± 0.11	1982.63 ± 0.09	2036.53 ± 0.18	2085.86 ± 0.55
16	1802.22 ± 0.11	1848.96 ± 0.08	1898.21 ± 0.14	1942.27 ± 0.37	2044.36 ± 0.08	2098.11 ± 0.09	2152.66 ± 0.13	2202.49 ± 0.51
17	1904.54 ± 0.07	1952.13 ± 0.07	2001.62 ± 0.10	2045.71 ± 0.26	2159.61 ± 0.09	2214.10 ± 0.08	2269.10 ± 0.11	2319.40 ± 0.30
18	2007.55 ± 0.08	2055.47 ± 0.07	2105.16 ± 0.08	2150.90 ± 0.21	2275.94 ± 0.07	2331.18 ± 0.07	2386.26 ± 0.09	2437.21 ± 0.18
19	2110.84 ± 0.07	2159.00 ± 0.07	2208.80 ± 0.10	2253.80 ± 0.46	2392.77 ± 0.07	2448.21 ± 0.06	2503.41 ± 0.07	2554.27 ± 0.19
20	2214.16 ± 0.09	2262.53 ± 0.08	2312.57 ± 0.13	2357.14 ± 0.23	2509.70 ± 0.06	2565.37 ± 0.06	2620.41 ± 0.08	2671.89 ± 0.20
21	2317.24 ± 0.08	2366.22 ± 0.10	2416.10 ± 0.19	2462.21 ± 0.44	2626.39 ± 0.07	2682.35 ± 0.07	2737.68 ± 0.10	2789.57 ± 0.36
22	2420.84 ± 0.12	2470.28 ± 0.13	2520.22 ± 0.28	2570.63 ± 1.23	2743.38 ± 0.08	2799.70 ± 0.08	2855.23 ± 0.19	2907.01 ± 0.53
23	2524.70 ± 0.20	2575.06 ± 0.19	2624.34 ± 0.38	2671.71 ± 1.28	2860.48 ± 0.15	2917.76 ± 0.14	2972.96 ± 0.26	3026.60 ± 0.71
24	2629.18 ± 0.27	2679.49 ± 0.26	2729.50 ± 0.80	2769.76 ± 2.59	2978.33 ± 0.16	3035.48 ± 0.20	3092.39 ± 0.54	3144.19 ± 1.18
25	2734.04 ± 0.50	2784.86 ± 0.43	2841.07 ± 1.41	2880.85 ± 2.89	3096.41 ± 0.44	3154.00 ± 0.32	3211.21 ± 1.53	3270.51 ± 3.99
26	2836.97 ± 0.59	2889.25 ± 0.63	2944.76 ± 4.42	2983.32 ± 6.73	3215.32 ± 0.91	3274.65 ± 0.72	3326.74 ± 1.54	3384.17 ± 9.66
27	2944.29 ± 2.14	2997.94 ± 1.27	...	...	3333.01 ± 0.74	3393.30 ± 0.63	...	...
28	...	...	3145.65 ± 2.00	3202.02 ± 9.71	...	...	...	...
29	3151.94 ± 0.64	3211.30 ± 3.36	...	...	...	...	...	...

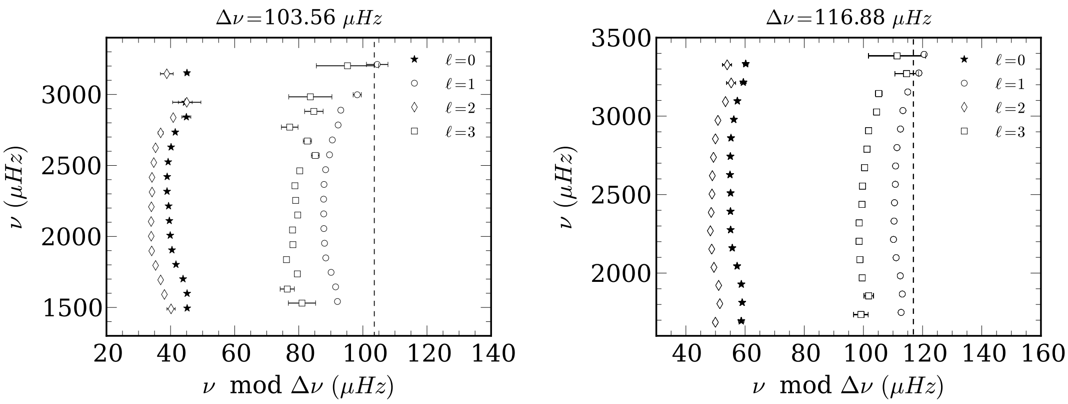

Fig. 4.2 - Observational échelle diagrams of 16 Cyg A and B. The values of the large separation, obtained from a linear fit to the radial modes, are also shown. The diagrams are duplicated at $\Delta\nu$, as shown by the dashed line.

4.3 Model fitting

The coupling between the MESA stellar evolution code and the ADIPLS adiabatic oscillation code allows for the calculation of pulsation frequencies during the evolution of the stellar models. The model frequencies can then be compared to the observed ones at each point in the evolutionary tracks. Using also other constraints like observed values of T_{eff}, $L/L_{\odot}$ and $[Fe/H]_s$ or asteroseismic quantities like the large separation and the frequency of maximum power, we can try to find the best-fitting model and the parameters that describe it, such as its mass and age.

Several approaches are available in MESA to find the best model, including grid-based searches and automatic χ^2 minimization algorithms. The user has control over which constraints are considered and the relative weights of each one. The general form of the χ^2 which should be minimized is given by

$$\chi^2 = W_{\text{spec}}\, \chi^2_{\text{spec}} + W_{\text{seismic}}\, \chi^2_{\text{seismic}} \tag{4.1}$$

where W_{spec} and W_{seismic} are the weights for the spectroscopic and seismic components respectively.

The full description of how MESA actually performs the automatic search[‡] can be found in [Paxton et al., 2013] and will not be repeated here. The model frequencies calculated by ADIPLS are corrected for surface effects using the empirical power-law correction proposed by [Kjeldsen et al., 2008]. In principle, for a particular combination

[‡]Note that in newer versions of the code (as the one used in this work) the Hooke & Jeeves algorithm has been replaced with a more robust simplex algorithm [Nelder and Mead, 1965]. Everything else operates in the same way.

of evolution and pulsation codes the power-law exponent (usually denoted b) should be determined from a solar calibration which would define the physics to be used in the models. However, it has been shown that variations of b do not affect the mean density of the models [Kjeldsen et al., 2008] and one unique value can be used to model all stars. Therefore we set this parameter to the standard value of 4.9 that was obtained in the original work. The seismic component of the χ^2 which contains the frequencies has the form described in [Brandão et al., 2011, eq. (11)].

The physics included in each model is the following: the equation of state tables are based on the 2005 update of the OPAL EOS tables [Rogers and Nayfonov, 2002], radiative opacities are taken from OPAL [Iglesias and Rogers, 1993, 1996] and [Ferguson et al., 2005], and nuclear reaction rates from NACRE [Angulo et al., 1999]. Convection is treated with the standard mixing-length theory as presented in [Cox and Giuli, 1968], without overshoot. Particle diffusion and gravitational settling are included using the method and coefficients of [Thoul et al., 1994]. Each physics module is described in more detail in [Paxton et al., 2011] and the full list of input parameters used in our work can be found at the url `https://www.astro.up.pt/~jfaria/msc-thesis` for future reference and reproducibility.

It is important to also describe recent updates to the code that allow the frequency ratios described in Section 2.3.1 to be included in the fitting process. For each model in the evolutionary tracks, the *uncorrected* model frequencies[§] are used to obtain the current values of the model ratios which are then compared to the observed ones. This is included in the seismic component of the χ^2 with an individual weight that is also user-defined. We only include the r_{02} and r_{010} ratios.

Note that by calculating the ratios with frequencies to which the surface correction has not yet been applied, we are removing the undesired bias that results from this *ad-hoc* correction. Also note that we do not take into account the correlations present in the r_{010} ratios. To do that we would have to include the covariance matrix in the χ^2. The position of the minimum in the parameter space (the parameters of the best model) will not change because of this.

In principle, by including in the fit only the frequency ratios and not the frequencies themselves, the converged model would be a better representation of the interior of the star, less biased by the incorrect modelling of the near-surface layers and by the empirical surface correction [Silva Aguirre et al., 2013]. In practice, the ratios alone cannot guarantee a clear identification of the mode degrees and so at least one radial

[§]Actually, in the default version of the code available for download, the *corrected* frequencies are used to calculate the ratios. We believe that using the frequencies *before applying the surface correction* is more accurate and more inline with our justification for using the ratios. A custom version of MESA that uses uncorrected frequencies was thus used in this work (the changes will be subject to community review to be included in the main version).

frequency would always have to be included to identify the modes. We have chosen to always include the available frequencies‖ and give a weight of $1/2$ to the frequencies and $1/2$ to the ratios in the seismic component. The values of $\Delta\nu$ and ν_{max} are only used as a guide to the conditional calculation of frequencies for some models*. The spectroscopic constraints are the observed values of T_{eff}, $L/L_{\odot}$, $\log(g)$ and $[Fe/H]_s$ (see Table 4.1). The final χ^2 is calculated from the seismic component (given $2/3$ of the weight as in [Metcalfe et al., 2012]) and the spectroscopic component, following Eq. (4.1).

For a complete search we set the mass M, initial helium abundance Y, initial metallicity $[Fe/H]_i$ and mixing length parameter α as free parameters. In some searches we have also considered an overshoot parameter f_{ov} to be free which, as will be shown, provides marginally better results. The way overshoot is implemented in MESA is different from other codes as it does not take into account changes in the energy transport mechanism in the overshoot region. Basically, in this framework, overshoot only acts as a source of extra diffusive mixing and including it or not does not explicitly change the temperature gradient [see Herwig, 2000, and references there in].

The age of the best model in a evolutionary track corresponds to the lowest χ^2 value for that track. We do not make an attempt to quantify the uncertainties with which the model parameters are derived.

Besides providing the best model parameters obtained from MESA, in this section our results are also compared with the work of Metcalfe et al. [2012, henceforth M12].

4.3.1 *16 Cyg A*

In Table 4.4, the parameters of the two best models for the A component, either considering overshoot as a free parameter or setting f_{ov} to zero, are presented. The evolutionary tracks, from the pre-main sequence phase until the age of the best model, are shown in the HR diagram in Figure 4.3 together with the observational constraints. The solid, dashed and dotted black lines show $1\sigma, 2\sigma$ and 3σ uncertainties in T_{eff} and $\log g$.

Letting f_{ov} vary during the search results in a model with similar overall χ^2 and seismic parameters. The biggest differences to the best model with $f_{ov} = 0$ is in the spectroscopic part, where including overshoot seems to have a positive effect. We present additional results only for the model where overshoot was included.

‖In the case of 16 Cyg A, we did not consider the very last modes of all angular degrees due to radial order identification issues.

*Calculating model oscillation frequencies is a computationally costly process that should be avoided in models which are clearly far from the best one, i. e. are not close to the observed values of $\Delta\nu$ and ν_{max}.

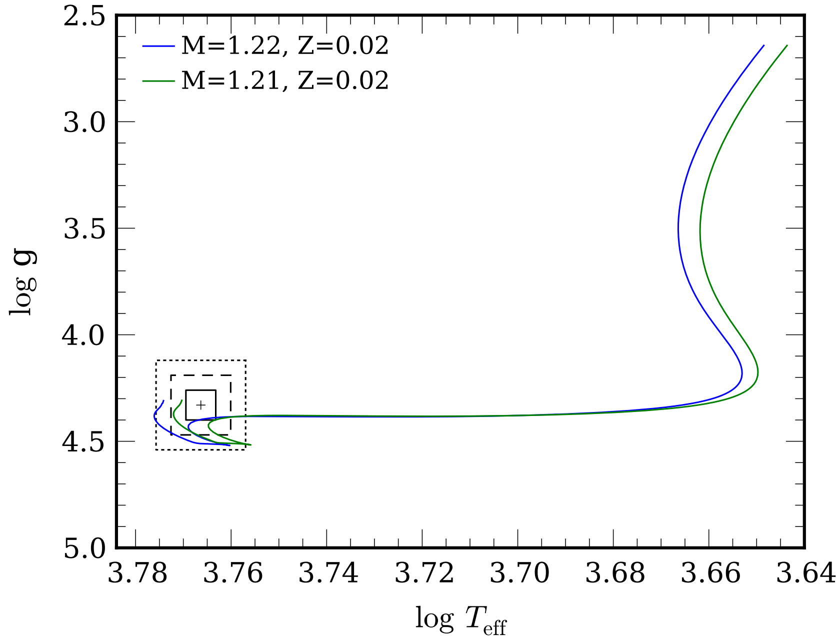

Fig. 4.3 - Evolutionary tracks of the best models for 16 Cyg A, obtained with the overshoot parameter set to zero (blue) and as a free parameter of the fit (green). The observational constraints and $1\sigma, 2\sigma, 3\sigma$ boxes are also shown.

The observed and model frequencies are shown in the échelle diagram of Figure 4.4 and the large separations $\Delta\nu_{n,\ell}$ in Figure 4.5. In these quantities, the best model fits most observed values within their 2σ uncertainties.

In the ratios, especially the r_{010}, some discrepancies are visible (left panel of Figure 4.7). The uncertainties in the data increase rapidly with frequency, especially above 2500μHz. The model ratios are not able to reproduce the upwards turn that is present in the observed ratios which is indicative of differences in the inner structure of the model and the real star.

4.3.2 *16 Cyg B*

For the B component, the parameters of the two best models, again either letting f_{ov} vary or not, are shown in Table 4.4. The right panel of Figure 4.4 shows the échelle diagram for the model where f_{ov} was free. Most seismic observations are well fitted, as is the case of the small frequency separations d_{010} (constructed in the same way as r_{010}) and the ratios, respectively shown in Figure 4.6 and in the right panel of Figure 4.7. Overall, the seismic results for this star are clearly in better agreement with the observations. However, some spectroscopic values such as the effective temperature, are outside the 2σ observational uncertainties.

4.3.3 *Comparison with previous results*

In Table 4.4 are also shown the parameters derived by [M12] for both stars. In that work both stars were modelled by fitting the individual frequencies obtained from three months of *Kepler* data and the spectroscopic constraints from Ramírez et al. [2009]. Instead of using just one stellar evolution code and fitting method, a total of seven models were obtained for each star. Each of these models was calculated with a different numerical code, and includes slightly different input physics and assumptions. An ensemble result (average of all the models) was also calculated.

Our best model results are close to the ensemble average in the case of 16 Cyg B, but for the A component, they do not compare as well. Our models of 16 Cyg A are more massive and have a bigger radii (and thus a younger age to be able to match the observed large separation).

There are many possible explanations for these differences. This is one of the first times MESA is being used in the context of asteroseismic model fitting. From the analysis in [M12], it is obvious that a simple change of the stellar evolution code, even with similar fitting methods, can impact the resulting best parameters. In this regard, we should also note that MESA's χ^2 minimization algorithms are not global and thus are more prone to getting stuck in local minima than, for example, the genetic algorithm used in AMP[6]. In addition, we have considered a longer time series of *Kepler* data and have included the frequency ratios in the analysis. We made an effort to include every available frequency, despite its observational error.

In our analysis, the chemical composition and age of one component was not constrained to match the other's. While we do obtain some agreement in the ages, especially when we let f_{ov} vary, the initial Helium abundances of the models are somewhat different. Assuming a common origin for the binary system, these parameters should agree between the components, which raises one important question: should we expect the best models to agree with each other in stellar ages and initial chemical compositions or should we force this agreement, based on *a priori* assumptions about the binary system? It is possible to devise a process where both components of the binary undergo seismic fitting at the same time, using MESA's ability to evolve more than one stellar model at the same time. This is something that should be further explored in the future for the cases of 16 Cyg as well as other binary systems.

[6] Of course a global minimization algorithm requires many more function evaluations (stellar evolution tracks) thus involving a much greater computational cost.

Table 4.4 - Model fitting results for 16 Cyg A & B. Adapted from [M12].

	16 Cyg A						16 Cyg B					
	$R/R_\odot$	$M/M_\odot$	t(Gyr)	Z_i	Y_i	α	$R/R_\odot$	$M/M_\odot$	t(Gyr)	Z_i	Y_i	α
This work												
$f_{ov} = 0$	1.286	1.23	6.16	0.029	0.237	2.17	1.135	1.09	6.93	0.020	0.244	2.03
f_{ov} free	1.279	1.21	6.29	0.028	0.239	2.06	1.125	1.07	6.69	0.0198	0.262	2.00
M12												
ensemble	1.243	1.11	6.9	0.024	0.25	2.00	1.127	1.07	6.7	0.023	0.25	1.92
AMP	1.236	1.10	6.5	0.022	0.25	2.06	1.123	1.06	5.8	0.020	0.25	2.05
ANKİ	1.260	1.14	6.4	0.024	0.26	1.94	1.138	1.08	6.4	0.022	0.26	1.94
ASTEC1	1.237	1.10	7.5	0.023	0.25	2.00	1.121	1.05	7.3	0.021	0.25	2.00
ASTEC2	1.235	1.10	6.8	0.022	0.25	2.00	1.134	1.09	6.3	0.025	0.25	2.00
CESAM	1.253	1.14	7.0	0.027	0.24	0.72	1.136	1.09	6.9	0.025	0.24	0.73
Geneva	1.236	1.10	6.7	0.024	0.26	1.80	1.122	1.06	6.7	0.024	0.26	1.80
YREC	1.244	1.11	6.9	0.026	0.26	2.08	1.121	1.05	6.9	0.022	0.26	1.84

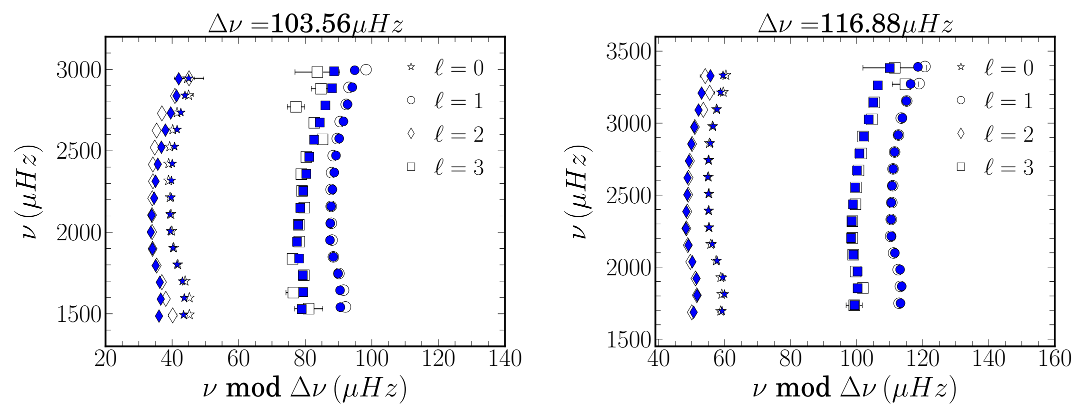

Fig. 4.4 - Échelle diagrams with the best model frequencies (filled blue symbols), for models of 16 Cyg A (left) and B (right), with f_{ov} as a free parameter. The observed frequencies included in the modelling are shown as open symbols with the corresponding error bars. Values of the large separation (see Table 4.2) are also shown and the diagrams are duplicated at $\Delta\nu$.

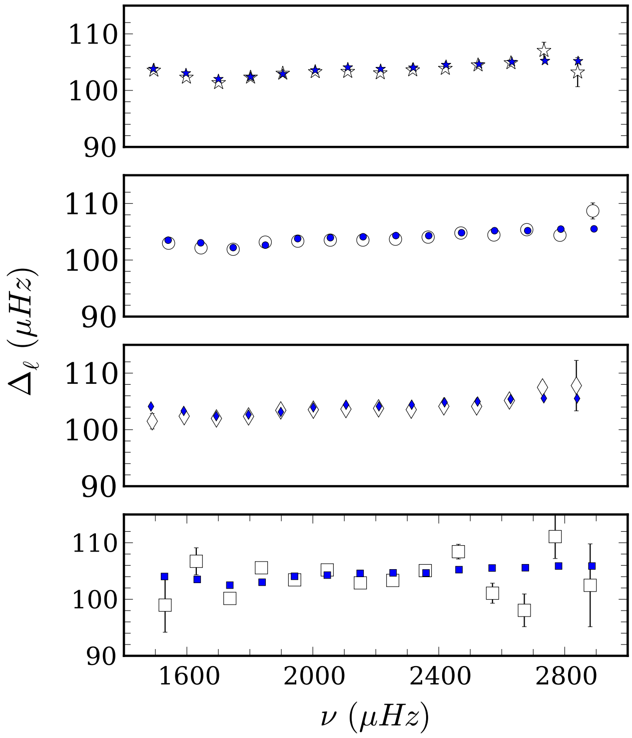

Fig. 4.5 - Large frequency separations, calculated with Eq. (2.10) for 16 Cyg A. The best model separations are the filled blue symbols and the observed values the open symbols with 1σ errorbars. Different mode degrees are shown from top to bottom panels with the same symbol code as before.

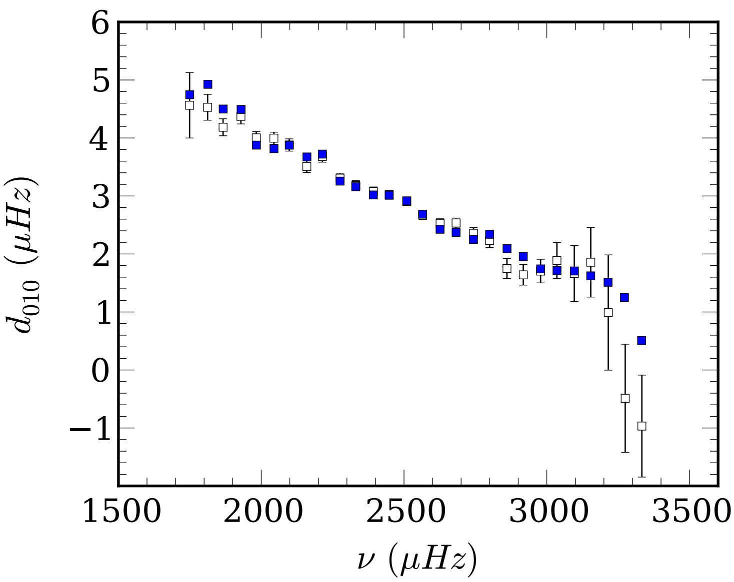

Fig. 4.6 - Small frequency separation d_{010} for the best model (f_{ov} free) of 16 Cyg B and matching observed values with 1σ errorbars, as a function of frequency.

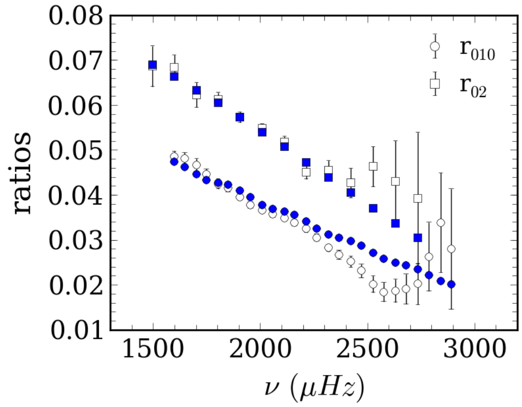

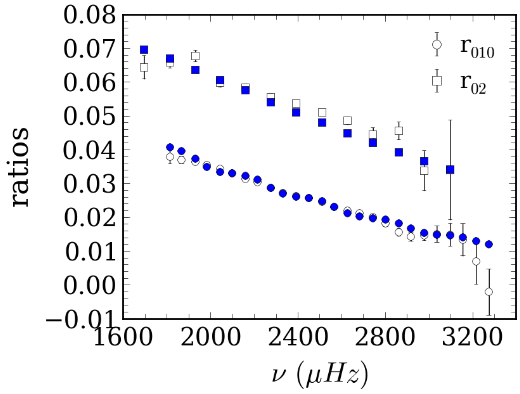

Fig. 4.7 - Frequency ratios r_{02} and r_{010} as a function of frequency, from the best models (filled blue symbols) and from observations (open symbols), for 16 Cyg A and B (left and right panels, respectively).

4.4 Acoustic glitches

Having validated both methods for the detection of the acoustic glitches (Section 3.4), we now apply them to the data of 16 Cyg A & B.

We start with Method 1 and present the results of fitting Eq. (3.15) to the set of 64 and 60 frequencies for the A and B components respectively. Figure 4.8 shows the results of the fits in the top panels, with modes of different degrees represented by the same symbols as in Page vii, and with error bars corresponding to the quoted observational uncertainties. The fitted smooth component has already been removed from the frequencies. In the bottom panels, the individual components from the HeIIZ and the BCZ are shown.

After the successful convergence of Method 1, a total of 5000 Monte Carlo realizations of the frequencies were produced to estimate the errors in the derived parameters. The final distributions of some of the parameters are presented in Figures 4.9 and 4.10 and in Table 4.5 we quote the mean, median and standard deviation for each parameter. The resulting values of the acoustic locations from Method 1 are

$$\tau^A_{\mathrm{HeIIZ}} = 953.08 \pm 13.75 \text{ s} \qquad \tau^B_{\mathrm{HeIIZ}} = 784.70 \pm 13.09 \text{ s}$$
$$\tau^A_{\mathrm{BCZ}} = 2828.47 \pm 136.82 \text{ s} \qquad \tau^B_{\mathrm{BCZ}} = 2534.28 \pm 153.99 \text{ s}$$

Using Method 2, we fit the functional form (3.16) to a total of 52 observed second differences for both components. The fits are shown in Figure 4.11 with the same color and symbol codes as before. Individual components of the signal, created by the HeIIZ and the BCZ are represented by dashed and solid lines, respectively, in the bottom panels.

The distributions of the fitted parameters, obtained from 5000 Monte Carlo realizations of the *frequencies*, are shown in the histograms of Figures 4.12 and 4.13 and their

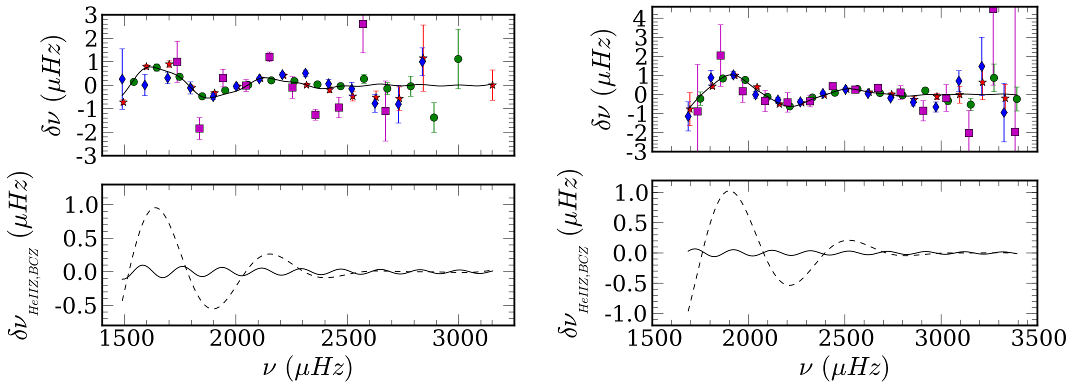

Fig. 4.8 - Results of applying Method 1 to the frequencies of 16 Cyg A (left) and B (rigth). The symbols in the upper panels denote the observed frequencies after the smooth component has been removed (different ℓ with the same color code as before) and the solid curve is the fit with Eq. (3.15). The bottom panels show the individual components originating from the HeIIZ (dashed line) and the BCZ (solid line).

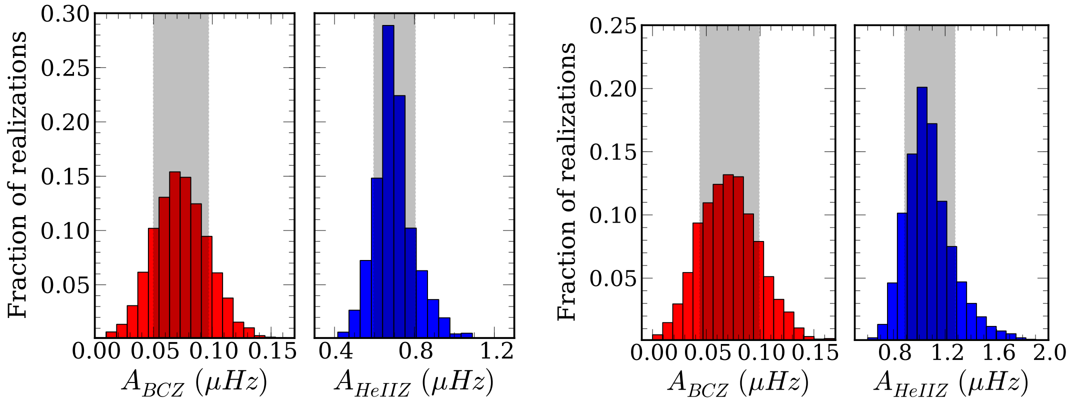

Fig. 4.9 - Histograms of the fitted values of A_{BCZ} and A_{HeIIZ} for 5000 Monte Carlo realizations of the frequencies of 16 Cyg A (left) and B (right). The shaded areas show the 1σ region around the means of the distributions.

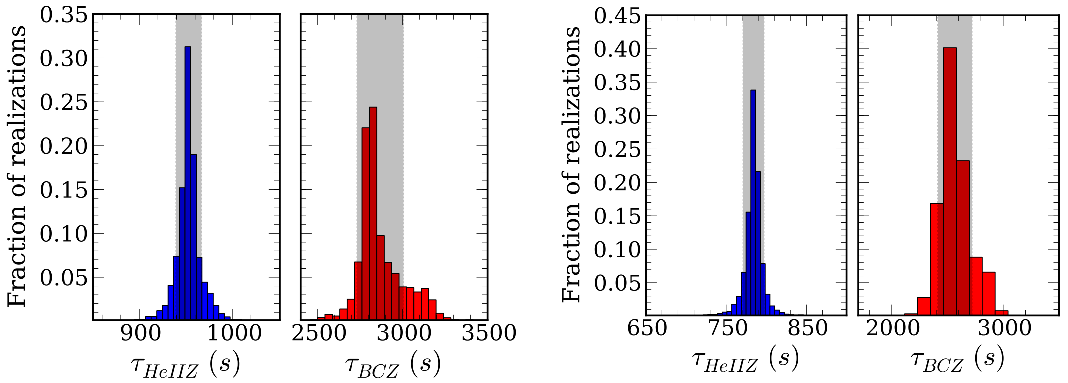

Fig. 4.10 - Histograms of the fitted values of τ_{HeIIZ} and τ_{BCZ} for 5000 Monte Carlo realizations of the frequencies of 16 Cyg A (left) and B (right). The shaded areas show the 1σ region around the means of the distributions.

Table 4.5 - Properties of the parameter distributions from Monte Carlo simulations of the fit to the frequencies.

Method 1		mean	median	σ
16 Cyg A	τ_{BCZ}	2868.15	2828.47	136.82
	τ_{HeIIZ}	953.07	953.08	13.75
	A_{BCZ}	0.073	0.073	0.024
	A_{HeIIZ}	0.70	0.69	0.10
	β	176.29	176.78	9.45
16 Cyg B	τ_{BCZ}	2566.83	2534.28	153.99
	τ_{HeIIZ}	784.08	784.70	13.09
	A_{BCZ}	0.072	0.071	0.028
	A_{HeIIZ}	1.08	1.05	0.20
	β	159.27	159.40	6.81

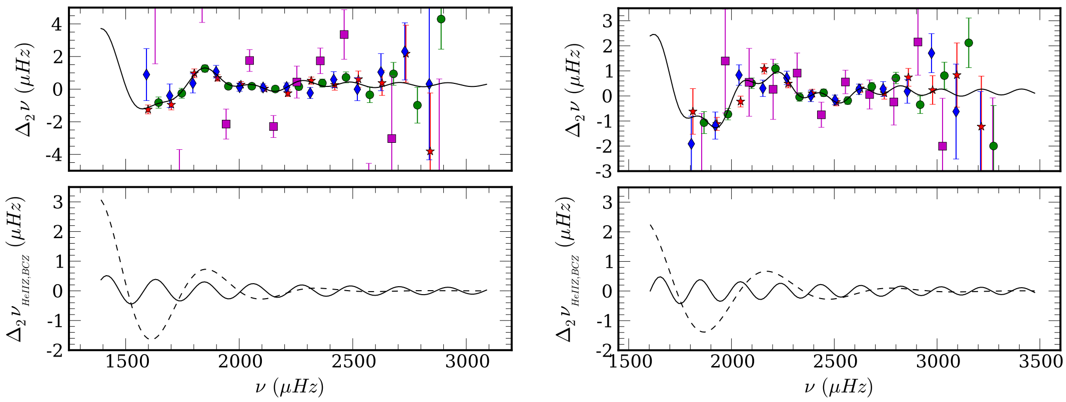

Fig. 4.11 - Method 2 results for the second differences of 16 Cyg A (left) and B (rigth). The symbols in the upper panels denote the observed second differences $\Delta_2\nu_{n,\ell}$ (different ℓ with the same colors and symbols as before) and the solid curve is the fit with Eq. (3.16). The bottom panels show the individual components originating from the HeIIZ (dashed line) and the BCZ (solid line).

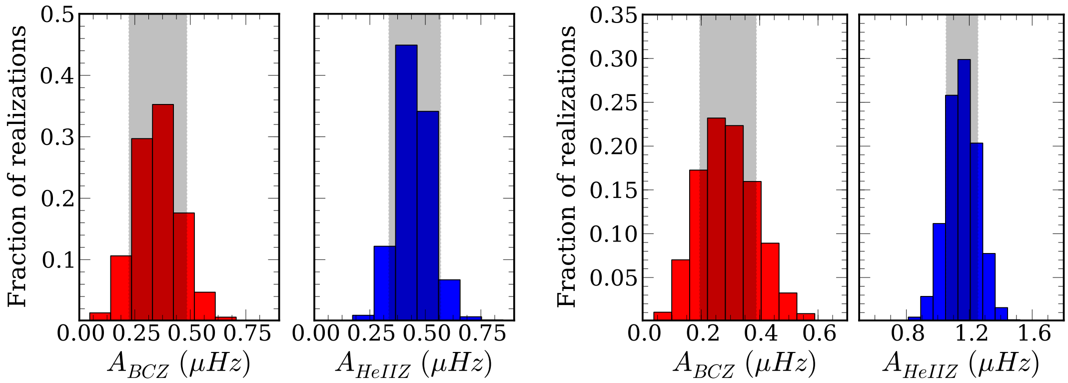

Fig. 4.12 - Histograms of the fitted values of A_{BCZ} and A_{HeIIZ}, obtained with Method 2, for 5000 Monte Carlo realizations of the frequencies of 16 Cyg A (left) and B (right). The shaded areas show the 1σ region around the means of the distributions.

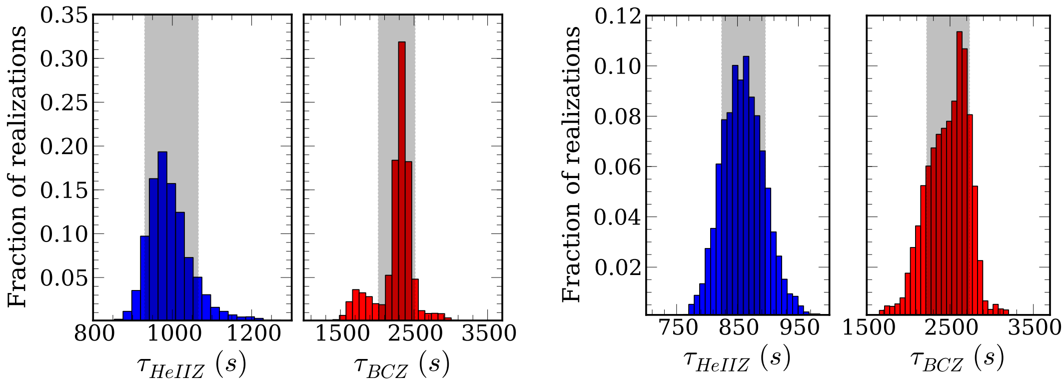

Fig. 4.13 - Histograms of the fitted values of τ_{HeIIZ} and τ_{BCZ} obtained with Method 2, for 5000 Monte Carlo realizations of the frequencies of 16 Cyg A (left) and B (right). The shaded areas show the 1σ region around the means of the distributions.

means, medians and standard deviations are in Table 4.6 with the following results for the locations of the glitches

$$\tau^A_{\text{HeIIZ}} = 985.80 \pm 67.47 \text{ s} \qquad \tau^B_{\text{HeIIZ}} = 859.00 \pm 35.75 \text{ s}$$
$$\tau^A_{\text{BCZ}} = 2317.28 \pm 249.56 \text{ s} \qquad \tau^B_{\text{BCZ}} = 2509.24 \pm 256.43 \text{ s}$$

With both Methods, the distribution of the values of τ_{BCZ} is more asymmetric than that of τ_{HeIIZ} (the mean and median are notably different), which can be explained by the difficulty in fitting a signal with such a small amplitude when compared to that of the HeIIZ signal.

We find a clear difference between the two Methods ($> 2\sigma$) for the inferred values of τ_{BCZ} in 16 Cyg A. In previous works, methods based on the second differences were found to suffer from the so-called "aliasing problem" [Mazumdar and Antia, 2001]. This

Table 4.6 - Properties of the parameter distributions from Monte Carlo simulations of the fit to the second differences.

Method 2		mean	median	σ
16 Cyg A	τ_{BCZ}	2264.36	2317.28	249.56
	τ_{HeIIZ}	997.82	985.80	67.47
	A_{BCZ}	0.35	0.35	0.13
	A_{HeIIZ}	0.45	0.45	0.12
	β	174.46	175.49	34.55
16 Cyg B	τ_{BCZ}	2476.69	2509.24	256.43
	τ_{HeIIZ}	859.90	859.00	35.75
	A_{BCZ}	0.29	0.29	0.10
	A_{HeIIZ}	1.15	1.15	0.10
	β	107.86	107.29	13.18

resulted in a significant fraction of fits with τ_{BCZ} equal to $T_0 - \tau_{\text{BCZ}}$, where T_0 is the total acoustic radius of the star. A good estimate for T_0 is $(2\Delta\nu_0)^{-1}$ which in this case is close to 4828 s. While the value obtained from Method 2 ($\sim 2317\,\text{s}$) cannot be explained completely by this phenomena (if we believe the value from Method 1 to be true, supported by the comparison with models in the next section) it lies close to the value corresponding to the Nyquist frequency of the data if we assume a sampling of $\Delta\nu_0$. Also, the histogram for τ_{BCZ} in Figure 4.13 shows clear bimodality, sugesting a problem with the fit of this parameter in 16 Cyg A.

4.4.1 *Glitches in the models*

The acoustic locations of the BCZ and HeIIZ glitches were determined in a completely model-independent way, with information extracted from the observed frequencies only. To test if the best models obtained in Section 4.3 adequately compare with the values determined from observations, we now reuse both detection Methods, to fit the signals in the model frequencies (and second differences). Only frequencies that correspond to the observed ones (the modes that were used in the stellar modeling) are considered. Also, the smoothing parameter from Method 1 was set to the same value as used for the observations.

In order to estimate an uncertainty for the parameters obtained for the models, the observational error of each frequency was assigned to the corresponding model frequency and a Monte Carlo simulation was performed on these data.

Table 4.7 shows the results of the fits for both stars and associated standard deviation for each parameter. We can compare these values with the ones from Tables 4.5 and

Table 4.7 - Signal parameters and associated uncertainties for the best MESA models (with overshoot), obtained from Methods 1 and 2.

		Method 1	Method 2
16 Cyg A	τ_{BCZ}	3141.54 ($\pm$ 52.87)	3118.84 ($\pm$ 117.62)
	τ_{HeIIZ}	847.70 ($\pm$ 5.42)	881.79 ($\pm$ 57.71)
	A_{BCZ}	0.11 ($\pm$ 0.03)	0.36 ($\pm$ 0.09)
	A_{HeIIZ}	0.45 ($\pm$ 0.05)	0.52 ($\pm$ 0.05)
	β	194.44 ($\pm$ 4.85)	133.76 ($\pm$ 15.71)
16 Cyg B	τ_{BCZ}	2772.01 ($\pm$ 57.36)	2747.63 ($\pm$ 89.47)
	τ_{HeIIZ}	875.16 ($\pm$ 13.25)	827.50 ($\pm$ 47.84)
	A_{BCZ}	0.14 ($\pm$ 0.03)	0.42 ($\pm$ 0.10)
	A_{HeIIZ}	0.91 ($\pm$ 0.07)	1.14 ($\pm$ 0.09)
	β	189.35 ($\pm$ 4.41)	121.67 ($\pm$ 14.11)

4.6 and also with the actual locations of the glitches that can be inferred from the temperature gradient ∇ inside the stars (the bump caused by Helium ionization and the discontinuity in the base of the convection zone will appear in this quantity). The adiabatic and radiative temperature gradients ∇_{ad} and ∇_{rad} are shown in Figure 4.15 together with ∇. It is important to note that we do not expect the location determined from the signals to exactly match the physical location in the models (this was briefly discussed in Section 3.1) and a difference up to $200\,$s between the two is to be expected.

A more graphical representation of these results is presented in Figure 4.14 where the amplitude of each signal is plotted against the acoustic depth, for each Method separately. Values obtained from observations (black squares) and from MESA models (blue circles) are shown together with parameters from a grid of representative models obtained with the YREC stellar evolution code [Verma et al., in prep.]. All values were obtained using the exact same fitting procedure. We see that the amplitudes of the signals are consistent in all cases. Both Methods also obtain consistent results for the locations of the BCZ and the HeIIZ from model frequencies. The detection of the BCZ signal in 16 Cyg A is clearly the most problematic and the BCZ locations determined in the models are only consistent with that obtained with Method 1 in the observations and not with the location obtained with Method 2.

The uncertainties in the parameters are often larger for Method 2, in part because of the increased errors in the second differences and also due to the presence of double peaks and asymmetries in the fitted parameter distributions.

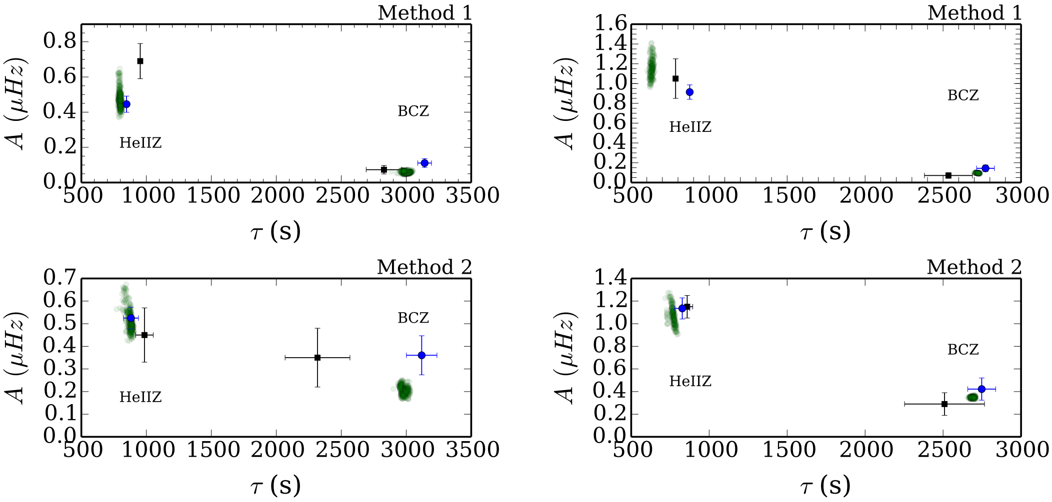

Fig. 4.14 - Amplitudes and acoustic locations obtained with both methods for 16 Cyg A (left) and B (right). Black squares represent observations, blue circles are obtained from the MESA best models and the green circles are for a grid of YREC representative models. Error bars are estimated from Monte Carlo realizations of the data.

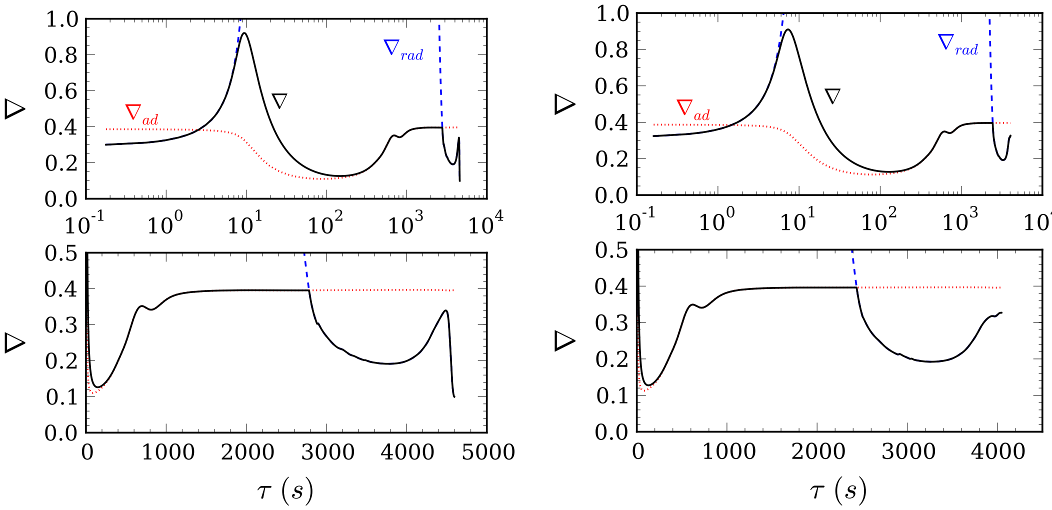

Fig. 4.15 - Temperature gradients for the best models of 16 Cyg A (left) and B (right) as a function of acoustic depth. The adiabatic $\nabla_{\rm ad}$ and radiative $\nabla_{\rm rad}$ gradients are shown with dotted red and dashed blue lines, respectively.

4.5 Calibrating the surface Helium abundance

The calibration of the helium abundance in the surface layers of the 16 Cyg stars, was one of the expected outcomes of this work. Here I present some preliminary results regarding that calibration, in which we try to use the existent relation between the HeIIZ signal that was detected in the second differences and the properties of the ionization region. Although definitely not a new subject in the case of the Sun [see Monteiro and Thompson, 2005, Houdek and Gough, 2011, and references therein] there have been yet no results on extending the calibration for other stars.

The parameters of the signal that are relevant to this calibration are the amplitudes A_{HeIIZ} and widths β_{HeIIZ} of the signals, because they are expected to be directly related to the local helium abundance. This is due to fact that the size of the depression in Γ_1 will be determined by how much Helium is available to be ionized.

However, many other aspects of the physics involved in the ionization region – in particular, the equation of state – will also affect the parameters so that the calibration will never be independent of uncertainties in the physics used in the models.

To attempt the calibration we use the fact that the product $A_{\text{HeIIZ}}\beta_{\text{HeIIZ}}$ is expected to be proportional to the Helium surface abundance Y_s [Monteiro and Thompson, 2005]. Several models of 16 Cyg A and B, with different global properties such as mass, age and different heavy element abundances have been constructed [Verma et al., in prep.]. They were divided in two groups with either the chemical mixture from Grevesse and Sauval [1998] (labeled "gs98") or from Asplund et al. [2009] (labeled "aspd"). For each model we have fitted Eq. (3.16) to the model second differences using Method 2. The same frequency range as the observations was used.

With the signal parameters and the value of Y_s for each model, the calibration can be done by studying what values of the surface Helium abundance reproduce the signal parameters coming from observations. We have determined the median of the distribution of $A_{\text{HeIIZ}}\beta_{\text{HeIIZ}}$ coming from the Monte Carlo simulations of Method 2. Figure 4.16 shows the results of the calibration for both 16 Cyg A and B.

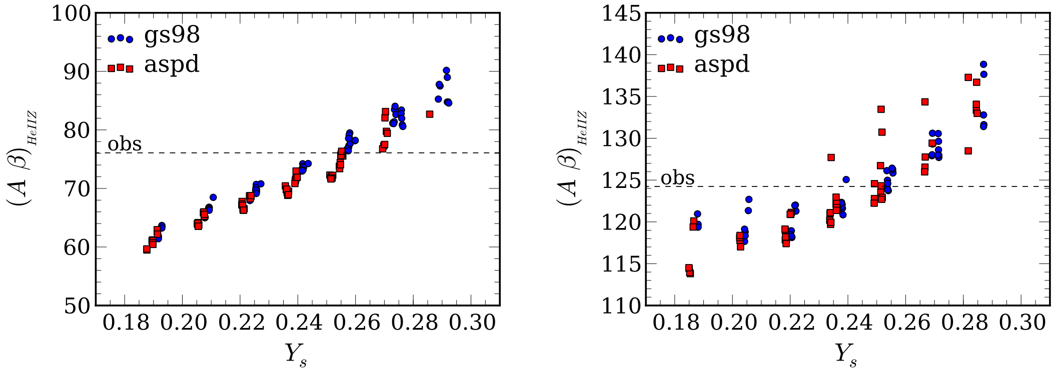

Fig. 4.16 - Calibration of the Helium surface abundance for 16 Cyg A (left) and B (right). The symbols show the quantity $A_{\text{HeIIZ}}\beta_{\text{HeIIZ}}$ obtained from the frequencies of models with different chemical mixtures, as function of model surface Helium abundance. The observational value from Monte Carlo simulations is also shown (labeled "obs").

A value of Y_s in the range $0.24 - 0.26$ is suggested by the observations, when considering models with these particular characteristics, although no extensive study of the uncertainties associated with the calibration has been carried out yet.

5

Conclusion

An asteroseismic study of the two stars 16 Cyg A and B was conducted, based on oscillation frequencies obtained from nine months of *Kepler* photometric time series data. This set of frequencies is of outstanding quality, with mean uncertainties under $1\,\mu$Hz and a total of 60 or more modes detected for each star. Several diagnostics that use combinations or intrinsic properties of the frequencies were studied in an attempt to extract useful information about the stellar interiors.

The ratios of small to large separations were added as a seismic constraint in the forward modeling approach with MESA. In principle, we could obtain models that better represent the interior regions of the stars because the ratios are virtually independent of the structure of the outer layers and also do not rely on the empirical surface correction, as do the frequencies. However, since the frequencies were also included in the χ^2, this advantage might be mitigated by an unknown bias caused by the correction which will still be present.

Also, the ratios (especially those of 16 Cyg A) show higher variability in the high frequency regime which can be an intrinsic behavior that is not being reproduced by the models, or an effect of the increased errors. The points with smaller frequency will contribute more to the component of the χ^2 that includes the ratios, because of their smaller uncertainties. It seems though that during the search for the best model, and probably because there is no model that matches closely the observed behavior, the higher frequency points are being "averaged out" (this is especially noticeable in the left panel of Figure 4.7). This might be introducing an unknown bias in the results. Nevertheless, the justification to include every available observed frequency, regardless of the associated uncertainty is still valid.

We have obtained two best models for each star (Table 4.4), either considering an overshoot parameter f_{ov} as a free parameter or setting it to zero. Two different and independent searches were performed to find the best fitting models, so that the effect of including overshoot mixing cannot be inferred from comparing the two resulting best models [on this subject see, e. g., Marques et al., 2004, 2005]. We find that the added degree of freedom from letting f_{ov} vary resulted in models in closer agreement with the spectroscopic constraints and that also agree in properties that should be common to both stars, like the stellar ages.

Since we did not use the same set of frequencies as Metcalfe et al. [2012] and also did not consider the same spectroscopic constraints, some differences in the best model parameters are to be expected (recent works show that such differences can even originate from a simple change in the fitting method [Gruberbauer et al., 2013]). It is nevertheless reassuring that the best models obtained from MESA are not completely discrepant from those obtained with other methods.

The abrupt changes in the stratification of a star, connected with the regions of ionization of helium and the base of the convection zone, were also studied in depth. These acoustic glitches produce a characteristic oscillatory signal in the oscillation frequencies that can be detected and characterized. In that way, we were able to extract information about the interior regions of the star where the signals originated from.

The development and improvement of two different methods to characterize the above mentioned signals are a cornerstone of this work. They fit to the frequencies or to the second differences an appropriate functional form for the signal and the resulting parameters describe, among other properties, an estimate of the acoustic locations of the glitches.

The amplitude of the signals in the second differences is enhanced relative to a smooth component that is present in both frequencies and second differences. This smooth component needs to be removed before fitting the signals and the two methods discussed here achieve this in different ways. Method 1 does not assume a functional form for the smooth function but it does depend on a parametric fit to remove it, introducing a parameter λ that is difficult to constrain. Method 2 assumes a simpler constant or polynomial function. We have determined that the fitted amplitudes (in representative models) do not show the magnification expected from theoretical calculations. This can be because the two methods do not remove exactly the same smooth function.

As a result, there is no clear advantage in using the second differences to detect the HeIIZ signal. For the BCZ signal there is an amplitude magnification but, as we see in Figure 4.14, the increased uncertainties on the second differences propagate to the fit parameters adding to the uncertainties in the latter.

Overall, both methods end up giving consistent results in most aspects, although Method 1 seems less prone to contamination in the smaller amplitude signal from the base of the convection zone and compares favorably with results from the MESA best models. Our conclusion is that both Methods benefit from the improvements studied and applied here and can provide interesting results for other solar-type stars.

With this methodology we have determined the acoustic depth of the base of the convection zone and the second helium ionization region for both stars. Another characteristic of the signal, that relates directly with the Helium abundance in the surface, was used to attempt a calibration of this quantity. We have obtained a range of values for Y_s which is favored by the observations. Although still work in progress, this calibration can provide a more direct way of determining the helium abundance of a star.

The outstanding data available from the *Kepler* mission is only now beginning to be fully exploited[†]. At the same time, the best methods to perform a complete and thorough analysis of these data, are still being devised. The goals of this work were to study and improve currently used diagnostics, in an attempt to learn more about the interiors of two particular stars. To the author's knowledge, it was the first time that MESA was used to perform asteroseismic model fitting (apart from the proof-of-concept example in Paxton et al. [2013]). We went beyond the more traditional approaches and explored the use of the frequency ratios as more precise proxies of the deep interiors of stars. In the future, we expect this approach to be improved upon and stellar models to come even closer to real stars. Additional work is still needed in developing methods that cancel the biases resulting from the deficient modelling of the near-surface layers, like the surface corrections applied to the frequencies.

On the study of acoustic glitches, we focused on two methods to extract and characterize the oscillatory signals present in the frequencies. A model independent measure of the acoustic locations of the base of the convection zone and of the Helium ionization region can be achieved with the methods. Preliminary results show that a calibration of the Helium surface abundance is also possible. The two components of the 16 Cyg binary were studied in depth with these methods. In the future, they should also be applied to other stars to, again, extract information about the stellar interiors. To facilitate reuse and reproducibility, the implementations of both methods will be made freely available online as open-source projects[‡].

To conclude, I believe the work presented here is important in the broader context of asteroseismology, in particular, of solar-type stars. But, as any scientific endeavor, it is far from complete and the question remains: how much more can we learn about stars?

[†]Despite the recent news that it might prove impossible to continue doing precision asteroseismology with *Kepler*, a wealth of data is still awaiting analysis

[‡]See `www.astro.up.pt/~jfaria/msc-thesis`

Bibliography

C. Aerts, J. Christensen-Dalsgaard, and D. W. Kurtz. *Asteroseismology*. Astronomy and Astrophysics Library. Springer, 1st edition, 2010. URL http://amazon.com/o/ASIN/1402051786/. (Cited on pages 7, 9, 11, and 12.)

C. Angulo, M. Arnould, M. Rayet, P. Descouvemont, D. Baye, C. Leclercq-Willain, A. Coc, S. Barhoumi, P. Aguer, C. Rolfs, R. Kunz, J. W. Hammer, A. Mayer, T. Paradellis, S. Kossionides, C. Chronidou, K. Spyrou, S. degl'Innocenti, G. Fiorentini, B. Ricci, S. Zavatarelli, C. Providencia, H. Wolters, J. Soares, C. Grama, J. Rahighi, A. Shotter, and M. Lamehi Rachti. A compilation of charged-particle induced thermonuclear reaction rates. *Nuclear Physics A*, 656:3–183, August 1999. doi: 10.1016/S0375-9474(99)00030-5. (Cited on page 38.)

T. Appourchaux, W. J. Chaplin, R. A. García, M. Gruberbauer, G. A. Verner, H. M. Antia, O. Benomar, T. L. Campante, G. R. Davies, S. Deheuvels, R. Handberg, S. Hekker, R. Howe, C. Régulo, D. Salabert, T. R. Bedding, T. R. White, J. Ballot, S. Mathur, V. Silva Aguirre, Y. P. Elsworth, S. Basu, R. L. Gilliland, J. Christensen-Dalsgaard, H. Kjeldsen, K. Uddin, M. C. Stumpe, and T. Barclay. Oscillation mode frequencies of 61 main-sequence and subgiant stars observed by Kepler. *Astronomy & Astrophysics*, 543:A54, July 2012. doi: 10.1051/0004-6361/201218948. (Cited on page 35.)

M. Asplund, N. Grevesse, A. J. Sauval, and P. Scott. The Chemical Composition of the Sun. *Annual Review of Astronomy and Astrophysics*, 47:481–522, September 2009. doi: 10.1146/annurev.astro.46.060407.145222. (Cited on page 51.)

A. Baglin, M. Auvergne, P. Barge, E. Michel, C. Catala, M. Deleuil, and W. Weiss. The CoRoT mission and its scientific objectives. In C. Dumitrache, N. A. Popescu, M. D. Suran, and V. Mioc, editors, *Fifty Years of Romanian Astrophysics*, volume 895 of *American Institute of Physics Conference Series*, pages 201–209, March 2007. doi: 10.1063/1.2720423. (Cited on page 3.)

I. M. Brandão, G. Doğan, J. Christensen-Dalsgaard, M. S. Cunha, T. R. Bedding, T. S. Metcalfe, H. Kjeldsen, H. Bruntt, and T. Arentoft. Asteroseismic modelling of the solar-type subgiant star β Hydri. *Astronomy & Astrophysics*, 527:A37, March 2011. doi: 10.1051/0004-6361/201015370. (Cited on page 38.)

M. Brodsky and S. V. Vorontsov. Asymptotic theory of intermediate- and high-degree solar acoustic oscillations. *The Astrophysical Journal*, 409:455–464, May 1993. doi: 10.1086/172678. (Cited on page 17.)

A.-M. Broomhall, W. J. Chaplin, G. R. Davies, Y. Elsworth, S. T. Fletcher, S. J. Hale, B. Miller, and R. New. Definitive Sun-as-a-star p-mode frequencies: 23 years of BiSON observations. *Monthly Notices of the Royal Astronomical Society*, 396:L100–L104, June 2009. doi: 10.1111/j.1745-3933.2009.00672.x. (Cited on page 27.)

C. Catala. Asteroseismology. Online, 2009. URL http://www.lesia.obspm.fr/perso/claude-catala/plato_web_files/asteroseismology.html. (Cited on page 11.)

W. J. Chaplin, Y. Elsworth, G. R. Isaak, K. I. Marchenkov, B. A. Miller, R. New, B. Pinter, and T. Appourchaux. Peak finding at low signal-to-noise ratio: low-l solar acoustic eigenmodes at n<= 9 from the analysis of BiSON data. *Monthly Notices of the Royal Astronomical Society*, 336:979–991, November 2002. doi: 10.1046/j.1365-8711.2002.05834.x. (Cited on page 12.)

W. J. Chaplin, H. Kjeldsen, J. Christensen-Dalsgaard, S. Basu, A. Miglio, T. Appourchaux, T. R. Bedding, Y. Elsworth, R. A. García, R. L. Gilliland, L. Girardi, G. Houdek, C. Karoff, S. D. Kawaler, T. S. Metcalfe, J. Molenda-Żakowicz, M. J. P. F. G. Monteiro, M. J. Thompson, G. A. Verner, J. Ballot, A. Bonanno, I. M. Brandão, A.-M. Broomhall, H. Bruntt, T. L. Campante, E. Corsaro, O. L. Creevey, G. Doğan, L. Esch, N. Gai, P. Gaulme, S. J. Hale, R. Handberg, S. Hekker, D. Huber, A. Jiménez, S. Mathur, A. Mazumdar, B. Mosser, R. New, M. H. Pinsonneault, D. Pricopi, P.-O. Quirion, C. Régulo, D. Salabert, A. M. Serenelli, V. Silva Aguirre, S. G. Sousa, D. Stello, I. R. Stevens, M. D. Suran, K. Uytterhoeven, T. R. White, W. J. Borucki, T. M. Brown, J. M. Jenkins, K. Kinemuchi, J. Van Cleve, and T. C. Klaus. Ensemble Asteroseismology of Solar-Type Stars with the NASA Kepler Mission. *Science*, 332:213–, April 2011. doi: 10.1126/science.1201827. (Cited on page 3.)

P. Charbonneau. Genetic Algorithms in Astronomy and Astrophysics. *The Astrophysical Journal Supplement*, 101:309, December 1995. doi: 10.1086/192242. (Cited on page 26.)

P. Charbonneau. Release Notes for PIKAIA 1.2. NCAR Technical Note 451, Boulder: National Center for Atmospheric Research, 2002. (Cited on page 27.)

J. Christensen-Dalsgaard. Some aspects of the theory of solar oscillations. *Geophysical and Astrophysical Fluid Dynamics*, 62:123–152, 1991. doi: 10.1080/03091929108229129. (Cited on page 8.)

J. Christensen-Dalsgaard. Helioseismology. *Reviews of Modern Physics*, 74:1073–1129, November 2002. doi: 10.1103/RevModPhys.74.1073. (Cited on page 2.)

J. Christensen-Dalsgaard. ADIPLS - the Aarhus adiabatic oscillation package. *Astrophysics and Space Science*, 316:113–120, August 2008. doi: 10.1007/s10509-007-9689-z. (Cited on page 4.)

W. D. Cochran, A. P. Hatzes, R. P. Butler, and G. W. Marcy. The Discovery of a Planetary Companion to 16 Cygni B. *The Astrophysical Journal*, 483:457, July 1997. doi: 10.1086/304245. (Cited on page 33.)

T. G. Cowling. The non-radial oscillations of polytropic stars. *Monthly Notices of the Royal Astronomical Society*, 101:367, 1941. (Cited on page 8.)

Arthur N. Cox, editor. *Allen's Astrophysical Quantities*. Springer, 4th edition, 4 2001. ISBN 9780387951898. URL http://amazon.com/o/ASIN/038795189X/. (Cited on page 34.)

John P. Cox and R. Thomas Giuli. *Principles of Stellar Structure*. Gordon and Breach, Science Publishers, 1968. (Cited on page 38.)

M. S. Cunha, C. Aerts, J. Christensen-Dalsgaard, A. Baglin, L. Bigot, T. M. Brown, C. Catala, O. L. Creevey, A. Domiciano de Souza, P. Eggenberger, P. J. V. Garcia, F. Grundahl, P. Kervella, D. W. Kurtz, P. Mathias, A. Miglio, M. J. P. F. G. Monteiro, G. Perrin, F. P. Pijpers, D. Pourbaix, A. Quirrenbach, K. Rousselet-Perraut, T. C. Teixeira, F. ThÃ©venin, and M. J. Thompson. Asteroseismology and interferometry. *Astronomy & Astrophysics Review*, 14:217–360, 2007. doi: 10.1007/s00159-007-0007-0. (Cited on pages 2 and 13.)

F.-L. Deubner and D. Gough. Helioseismology: Oscillations as a Daignostic of the Solar Interior. *Annual Review of Astronomy and Astrophysics*, 22:593–619, 1984. doi: 10.1146/annurev.aa.22.090184.003113. (Cited on page 8.)

S. Dodelson and M. D. Schneider. Simulation Covariance Error. *ArXiv e-prints*, April 2013. arXiv:1304.2593. (Cited on page 26.)

J. W. Ferguson, D. R. Alexander, F. Allard, T. Barman, J. G. Bodnarik, P. H. Hauschildt, A. Heffner-Wong, and A. Tamanai. Low-Temperature Opacities. *The Astrophysical Journal*, 623:585–596, April 2005. doi: 10.1086/428642. (Cited on page 38.)

R. A. García, S. Hekker, D. Stello, J. Gutiérrez-Soto, R. Handberg, D. Huber, C. Karoff, K. Uytterhoeven, T. Appourchaux, W. J. Chaplin, Y. Elsworth, S. Mathur, J. Ballot,

J. Christensen-Dalsgaard, R. L. Gilliland, G. Houdek, J. M. Jenkins, H. Kjeldsen, S. McCauliff, T. Metcalfe, C. K. Middour, J. Molenda-Zakowicz, M. J. P. F. G. Monteiro, J. C. Smith, and M. J. Thompson. Preparation of Kepler light curves for asteroseismic analyses. *Monthly Notices of the Royal Astronomical Society*, 414:L6–L10, June 2011. doi: 10.1111/j.1745-3933.2011.01042.x. (Cited on page 35.)

R. L. Gilliland, T. M. Brown, J. Christensen-Dalsgaard, H. Kjeldsen, C. Aerts, T. Appourchaux, S. Basu, T. R. Bedding, W. J. Chaplin, M. S. Cunha, P. De Cat, J. De Ridder, J. A. Guzik, G. Handler, S. Kawaler, L. Kiss, K. Kolenberg, D. W. Kurtz, T. S. Metcalfe, M. J. P. F. G. Monteiro, R. Szabó, T. Arentoft, L. Balona, J. Debosscher, Y. P. Elsworth, P.-O. Quirion, D. Stello, J. C. Suárez, W. J. Borucki, J. M. Jenkins, D. Koch, Y. Kondo, D. W. Latham, J. F. Rowe, and J. H. Steffen. Kepler Asteroseismology Program: Introduction and First Results. *Publications of the Astronomical Society of the Pacific*, 122:131–143, February 2010. doi: 10.1086/650399. (Cited on page 3.)

D. Gough. Comments on helioseismic inference. In Y. Osaki and H. Shibahashi, editors, *Progress of Seismology of the Sun and Stars*, volume 367 of *Lecture Notes in Physics, Berlin Springer Verlag*, page 281, 1990. doi: 10.1007/3-540-53091-6_93. (Cited on page 3.)

D. Gough and J. Toomre. Seismic observations of the solar interior. *Annual Review of Astronomy and Astrophysics*, 29:627–685, 1991. doi: 10.1146/annurev.aa.29.090191.003211. (Cited on page 2.)

D. O. Gough. Linear adiabatic stellar pulsation. In J.-P. Zahn and J. Zinn-Justin, editors, *Astrophysical Fluid Dynamics - Les Houches 1987*, pages 399–560, 1993. (Cited on page 9.)

D. O. Gough. An elementary introduction to the JWKB approximation. *Astronomische Nachrichten*, 328:273, March 2007. doi: 10.1002/asna.200610730. (Cited on page 9.)

G. Grec, E. Fossat, and M. A. Pomerantz. Full-disk observations of solar oscillations from the geographic South Pole - Latest results. *Solar Physics*, 82:55–66, January 1983. doi: 10.1007/BF00145545. (Cited on page 10.)

N. Grevesse and A. J. Sauval. Standard Solar Composition. *Space Science Reviews*, 85:161–174, May 1998. doi: 10.1023/A:1005161325181. (Cited on page 51.)

M. Gruberbauer, D. B. Guenther, K. MacLeod, and T. Kallinger. Bayesian Asteroseismology of 23 Solar-Like Kepler Targets. *ArXiv 1307.4218G*, July 2013. (Cited on page 54.)

H. M. Hauser and G. W. Marcy. The Orbit of 16 Cygni AB. *Publications of the Astronomical Society of the Pacific*, 111:321–334, March 1999. doi: 10.1086/316328. (Cited on page 34.)

F. Herwig. The evolution of AGB stars with convective overshoot. *Astronomy & Astrophysics*, 360:952–968, August 2000. (Cited on page 39.)

G. Houdek. Convection and oscillations. *Astronomische Nachrichten*, 331:998–1003, December 2010. doi: 10.1002/asna.201011445. (Cited on page 3.)

G. Houdek and D. O. Gough. An asteroseismic signature of helium ionization. *Monthly Notices of the Royal Astronomical Society*, 375:861–880, March 2007. doi: 10.1111/j.1365-2966.2006.11325.x. (Cited on pages 14, 20, 22, 23, 28, and 30.)

G. Houdek and D. O. Gough. On the seismic age and heavy-element abundance of the Sun. *Monthly Notices of the Royal Astronomical Society*, 418:1217–1230, December 2011. doi: 10.1111/j.1365-2966.2011.19572.x. (Cited on page 51.)

D. Huber, D. Stello, T. R. Bedding, W. J. Chaplin, T. Arentoft, P.-O. Quirion, and H. Kjeldsen. Automated extraction of oscillation parameters for Kepler observations of solar-type stars. *Communications in Asteroseismology*, 160:74, October 2009. (Cited on page 35.)

C. A. Iglesias and F. J. Rogers. Radiative opacities for carbon- and oxygen-rich mixtures. *The Astrophysical Journal*, 412:752–760, August 1993. doi: 10.1086/172958. (Cited on page 38.)

C. A. Iglesias and F. J. Rogers. Updated Opal Opacities. *The Astrophysical Journal*, 464:943, June 1996. doi: 10.1086/177381. (Cited on page 38.)

H. Kjeldsen, T. R. Bedding, and J. Christensen-Dalsgaard. Correcting Stellar Oscillation Frequencies for Near-Surface Effects. *The Astrophysical Journal Letters*, 683:L175–L178, August 2008. doi: 10.1086/591667. (Cited on pages 3, 37, and 38.)

K. I. Marchenkov and S. V. Vorontsov. Seismic probing of outer regions of the sun. *Soviet Astronomy Letters*, 133:149–154, May 1991. doi: 10.1007/BF00149836. (Cited on page 19.)

J. P. Marques, J. Fernandes, and M. J. P. F. G. Monteiro. The role of the time step and overshooting in the modelling of PMS evolution: The case of EK Cephei. *Astronomy & Astrophysics*, 422:239–245, July 2004. doi: 10.1051/0004-6361:20035693. (Cited on page 53.)

J. P. Marques, M. J. P. F. G. Monteiro, and J. Fernandes. Effects of convective overshooting in the PMS evolution of intermediate mass stars. In F. Favata, G. A. J. Hussain, and B. Battrick, editors, *13th Cambridge Workshop on Cool Stars, Stellar Systems and the Sun*, volume 560 of *ESA Special Publication*, page 795, March 2005. (Cited on page 53.)

J. P. Marques, M. J. P. F. G. Monteiro, and J. M. Fernandes. Grids of stellar evolution models for asteroseismology (cesam + posc). *Astrophysics and Space Science*, 316: 173–178, August 2008. doi: 10.1007/s10509-008-9786-7. (Cited on pages 33 and 34.)

A. Mazumdar and H. M. Antia. Seismic study of stellar convective cores. *Astronomy & Astrophysics*, 377:192–205, October 2001. doi: 10.1051/0004-6361:20011072. (Cited on page 47.)

A. Mazumdar, M. J. P. F. G. Monteiro, J. Ballot, H. M. Antia, S. Basu, G. Houdek, S. Mathur, M. S. Cunha, V. Silva Aguirre, R. A. García, D. Salabert, G. A. Verner, J. Christensen-Dalsgaard, T. S. Metcalfe, and W. J. Chaplin. Acoustic glitches in solar-type stars from Kepler. *Astronomische Nachrichten*, 333:1040–1043, December 2012. doi: 10.1002/asna.201211825. (Cited on pages 4, 22, 23, and 24.)

T. S. Metcalfe, W. J. Chaplin, T. Appourchaux, R. A. García, S. Basu, I. Brandão, O. L. Creevey, S. Deheuvels, G. Doğan, P. Eggenberger, C. Karoff, A. Miglio, D. Stello, M. Yıldız, Z. Çelik, H. M. Antia, O. Benomar, R. Howe, C. Régulo, D. Salabert, T. Stahn, T. R. Bedding, G. R. Davies, Y. Elsworth, L. Gizon, S. Hekker, S. Mathur, B. Mosser, S. T. Bryson, M. D. Still, J. Christensen-Dalsgaard, R. L. Gilliland, S. D. Kawaler, H. Kjeldsen, K. A. Ibrahim, T. C. Klaus, and J. Li. Asteroseismology of the Solar Analogs 16 Cyg A and B from Kepler Observations. *The Astrophysical Journal Letters*, 748:L10, March 2012. doi: 10.1088/2041-8205/748/1/L10. (Cited on pages 3, 35, 39, 41, 42, and 54.)

M. J. P. F. G. Monteiro and M. J. Thompson. Seismic analysis of the second ionization region of helium in the Sun - I. Sensitivity study and methodology. *Monthly Notices of the Royal Astronomical Society*, 361:1187–1196, August 2005. doi: 10.1111/j.1365-2966.2005.09246.x. (Cited on pages 4, 17, 20, 21, 23, 27, and 51.)

M. J. P. F. G. Monteiro, J. Christensen-Dalsgaard, and M. J. Thompson. Seismic study of overshoot at the base of the solar convective envelope. *Astronomy & Astrophysics*, 283:247–262, March 1994. (Cited on pages 17, 18, 20, 21, 23, 24, and 27.)

M. J. P. F. G. Monteiro, J. Christensen-Dalsgaard, and M. J. Thompson. Seismic study of stellar convective regions: the base of the convective envelope in low-mass stars.

Monthly Notices of the Royal Astronomical Society, 316:165–172, July 2000. doi: 10.1046/j.1365-8711.2000.03471.x. (Cited on page 23.)

J. A. Nelder and R. Mead. A Simplex Method for Function Minimization. *The Computer Journal*, 7(4):308–313, 1965. doi: 10.1093/comjnl/7.4.308. (Cited on page 37.)

H. Otí Floranes, J. Christensen-Dalsgaard, and M. J. Thompson. The use of frequency-separation ratios for asteroseismology. *Monthly Notices of the Royal Astronomical Society*, 356:671–679, January 2005. doi: 10.1111/j.1365-2966.2004.08487.x. (Cited on page 11.)

J. Patience, R. J. White, A. M. Ghez, C. McCabe, I. S. McLean, J. E. Larkin, L. Prato, S. S. Kim, J. P. Lloyd, M. C. Liu, J. R. Graham, B. A. Macintosh, D. T. Gavel, C. E. Max, B. J. Bauman, S. S. Olivier, P. Wizinowich, and D. S. Acton. Stellar Companions to Stars with Planets. *The Astrophysical Journal*, 581:654–665, December 2002. doi: 10.1086/342982. (Cited on page 33.)

B. Paxton, L. Bildsten, A. Dotter, F. Herwig, P. Lesaffre, and F. Timmes. Modules for Experiments in Stellar Astrophysics (MESA). *The Astrophysical Journal Supplement*, 192:3, January 2011. doi: 10.1088/0067-0049/192/1/3. (Cited on pages 4 and 38.)

B. Paxton, M. Cantiello, P. Arras, L. Bildsten, E. F. Brown, A. Dotter, C. Mankovich, M. H. Montgomery, D. Stello, F. X. Timmes, and R. Townsend. Modules for Experiments in Stellar Astrophysics (MESA): Giant Planets, Oscillations, Rotation, and Massive Stars. *ArXiv e-prints*, January 2013. (Cited on pages 4, 37, and 55.)

D. Raghavan, T. J. Henry, B. D. Mason, J. P. Subasavage, W.-C. Jao, T. D. Beaulieu, and N. C. Hambly. Two Suns in The Sky: Stellar Multiplicity in Exoplanet Systems. *The Astrophysical Journal*, 646:523–542, July 2006. doi: 10.1086/504823. (Cited on page 33.)

I. Ramírez, J. Meléndez, and M. Asplund. Accurate abundance patterns of solar twins and analogs. Does the anomalous solar chemical composition come from planet formation? *Astronomy & Astrophysics*, 508:L17–L20, December 2009. doi: 10.1051/0004-6361/200913038. (Cited on pages 33, 34, and 41.)

F. J. Rogers and A. Nayfonov. Updated and Expanded OPAL Equation-of-State Tables: Implications for Helioseismology. *The Astrophysical Journal*, 576:1064–1074, September 2002. doi: 10.1086/341894. (Cited on page 38.)

I. W. Roxburgh and S. V. Vorontsov. Seismology of the Solar Envelope - the Base of the Convective Zone as Seen in the Phase Shift of Acoustic Waves. *Monthly Notices of the Royal Astronomical Society*, 268:880, June 1994. (Cited on page 19.)

I. W. Roxburgh and S. V. Vorontsov. The ratio of small to large separations of acoustic oscillations as a diagnostic of the interior of solar-like stars. *Astronomy & Astrophysics*, 411:215–220, November 2003. doi: 10.1051/0004-6361:20031318. (Cited on pages 11 and 12.)

S. C. Schuler, K. Cunha, V. V. Smith, L. Ghezzi, J. R. King, C. P. Deliyannis, and A. M. Boesgaard. Detailed Abundances of the Solar Twins 16 Cygni A and B: Constraining Planet Formation Models. *The Astrophysical Journal Letters*, 737:L32, August 2011. doi: 10.1088/2041-8205/737/2/L32. (Cited on page 33.)

V. Silva Aguirre, S. Basu, I. M. Brandão, J. Christensen-Dalsgaard, S. Deheuvels, G. Doğan, T. S. Metcalfe, A. M. Serenelli, J. Ballot, W. J. Chaplin, M. S. Cunha, A. Weiss, T. Appourchaux, L. Casagrande, S. Cassisi, O. L. Creevey, R. A. García, Y. Lebreton, A. Noels, S. G. Sousa, D. Stello, T. R. White, S. D. Kawaler, and H. Kjeldsen. Stellar Ages and Convective Cores in Field Main-sequence Stars: First Asteroseismic Application to Two Kepler Targets. *The Astrophysical Journal*, 769:141, June 2013. doi: 10.1088/0004-637X/769/2/141. (Cited on page 38.)

James O. Street, Raymond J. Carroll, and David Ruppert. A Note on Computing Robust Regression Estimates Via Iteratively Reweighted Least Squares. *The American Statistician*, 42(2):pp. 152–154, 1988. ISSN 00031305. URL http://www.jstor.org/stable/2684491. (Cited on page 26.)

M. Tassoul. Asymptotic approximations for stellar nonradial pulsations. *The Astrophysical Journal Supplement*, 43:469–490, August 1980. doi: 10.1086/190678. (Cited on page 9.)

M. Tassoul. Second-order asymptotic approximations for stellar nonradial acoustic modes. *The Astrophysical Journal*, 358:313–327, July 1990. doi: 10.1086/168988. (Cited on page 9.)

A. A. Thoul, J. N. Bahcall, and A. Loeb. Element diffusion in the solar interior. *The Astrophysical Journal*, 421:828–842, February 1994. doi: 10.1086/173695. (Cited on page 38.)

N. H. Turner, T. A. ten Brummelaar, H. A. McAlister, B. D. Mason, W. I. Hartkopf, and L. C. Roberts, Jr. Search for Faint Companions to Nearby Solar-like Stars using the Adaptive Optics System at Mount Wilson Observatory. *The Astrophysical Journal*, 121:3254–3258, June 2001. doi: 10.1086/321075. (Cited on page 33.)

Wasaburo Unno, Yoji Osaki, Hiroyasu Ando, H. Saio, and H. Shibahashi. *Nonradial Oscillations of Stars*. University of Tokyo Press, 2nd edition, 1989. URL http://adsabs.harvard.edu/abs/1989nos..book.....U. (Cited on page 7.)

F. van Leeuwen. Validation of the new Hipparcos reduction. *Astronomy & Astrophysics*, 474:653–664, November 2007. doi: 10.1051/0004-6361:20078357. (Cited on page 34.)

S. V. Vorontsov and V. N. Zharkov. Helioseismology - Theory and Interpretation of Experimental Data. *Astrophysics and Space Physics Reviews*, 7:1, 1989. (Cited on page 19.)

T. R. White, D. Huber, V. Maestro, T. R. Bedding, M. J. Ireland, F. Baron, T. S. Boyajian, X. Che, J. D. Monnier, B. J. S. Pope, R. M. Roettenbacher, D. Stello, P. G. Tuthill, C. D. Farrington, P. J. Goldfinger, H. A. McAlister, G. H. Schaefer, J. Sturmann, L. Sturmann, T. A. ten Brummelaar, and N. H. Turner. Interferometric radii of bright Kepler stars with the CHARA Array: θ Cygni and 16 Cygni A and B. May 2013. (Cited on pages 33, 34, and 35.)